Inference of Horizontal Temperature Gradients Using Passive Radiometric Methods

by Peter Olsson and Stephen K. Cox

Funding Agency: Army Research Office

Colorado State University

DEPARTMENT OF ATMOSPHERIC SCIENCE

PAPER NO.
447

INFERENCE OF HORIZONTAL TEMPERATURE GRADIENTS USING PASSIVE RADIOMETRIC METHODS

Peter Olsson
and
Stephen K. Cox

Department of Atmospheric Science
Colorado State University
Fort Collins, CO 80523

August, 1989

Atmospheric Science Paper No. 447

ABSTRACT

INFERENCE OF HORIZONTAL TEMPERATURE GRADIENTS USING PASSIVE RADIOMETRIC METHODS

There exist many situations in nature where relatively strong horizontal temperatur gradients are present in the boundary layer. The purpose of this work is to investigat the impact of horizontal temperature gradients on the infrared radiance properties c the boundary layer and devise a scheme for inferring the gradient magnitude from thes radiance properties.

The temperature and spectral dependence of the radiance of various atmospheri constituents are examined and the IR portion of the spectrum $500cm^{-1} \leq \nu \leq 800cm^{-}$ is shown to be most sensitive to temperature induced radiance changes. The two importan radiating gases at these wavenumbers are CO_2 and H_2O. The spectral radiative propertie of these constituents are discussed. The variability of the water vapor mixing ratio is show to be an important factor in this remote sensing application. A model is discussed whic numerically estimates the radiance of the boundary layer in the presence of a horizont temperature gradient. The results of this model demonstrate the possibility of estimatin the gradient magnitude from narrow band azimuthally scanned radiance measurements

Two parameters, the attenuation length and the centered normalized radiance, a introduced and their relationship to the gradient magnitude is explored. Using the parameters, a method is developed which permits the inference of temperature gradie magnitude from infrared radiance measurements and local pressure, temperature and mi ing ratio values. The success of this technique is demonstrated by the accurate recove of gradient magnitudes from calculated radiance data. Finally, consideration is given

sources of error and uncertainty in the measurement process and the impact of these on the inference of the gradient magnitude.

ACKNOWLEDGEMENTS

This research was funded by the Department of Defense–Army Research Office Grant DAAL03–86–K–0175/P00010 and the Department of Defense–Office of Naval Research N00014–87–K–0228/P00002.

CONTENTS

LIST OF FIGURES

LIST OF TABLES

Chapter 1

INTRODUCTION

There exist many situations in nature where relatively strong horizontal temperature gradients are present. These include, but are not limited to, frontal boundaries on the synoptic scale. On a smaller scale such gradients may develop as transient phenomena in the boundary layer when differential surface heating occurs. Small scale advection forced by mountain and valley circulations and downbursts of cold air from vigorously precipitating thunderstorms can create strong temperature variations over a short distance. In urban environments such gradients often arise in the nocturnal boundary layer due to the large heat capacity of man-made structures as contrasted with natural surfaces. The horizontal scale of these gradients can range from tens of meters in the case of differential surface heating to tens of kilometers in the case of synoptic scale features. The gradient magnitude can vary from .25° C/km to greater than 3° C/km.

Because of the role that these small scale temperature features play in the evolution of the planetary boundary layer they are of interest to a number of researchers. Advectively forced temperature gradients are often indicators of processes occuring outside of, and interacting with, the boundary layer. For these reasons it is desirable to accurately measure the magnitude and extent of such gradients.

Unfortunately many of these phenomena develop and dissipate rapidly and unpredictably. The atmosphere itself tends to mix these gradients out by random turbulent processes. Because of this transience reliable measurements can be quite difficult to make. The use of several thermometric devices for simultaneous measurement requires a priori knowlege as to when and where these gradients will occur. Also calibration errors and instrument noise among several simultaneously deployed devices can result in inconsistent measurements. Many of these problems can be minimized by using a single instrument for measurements at several points in space. For rapidly varying phenomena however, lack of simultaneity of measurements can also create invalid observations. Obviously it would be desirable to find a method of making such a measurement from a single location with a single instrument and yet include simultaneous information about the temperature field over a wide region of space. Radiometric techniques, which measure the electromagnetic radiation emitted by the atmospheric gases, offer just such a method.

It is well known that matter radiates electromagnetic energy as a function of its temperature. The exact distribution of this energy in the electromagnetic spectrum is determined by the material properties of the matter in question and on the Planck function:

$$B(\nu, T) = \frac{C_1 \nu^3}{e^{\frac{C_2 \nu}{T}} - 1} \tag{1.1}$$

where $C_1 = 2hc^2 = 1.1909 \times 10^{-12} cm^2\ st^{-1}$ and $C_2 = \frac{hc}{K} = 1.4388^\circ K\ cm$. The Planck function gives the radiance or energy density (in wavenumber space) per unit time per unit solid angle radiated by a perfect black body emitter. This places an upper bound on spectral black-body emission for a given temperature. Because of this relationship between temperature and radiance it is possible to remotely sense the temperature of an object far removed from the sensing device. Such methods have long been exploited by astrophysicists in determining the temperature of heavenly bodies (Swihart, 1968). Similar measurements from satellite platforms have allowed the remote sensing of surface temperatures on the earth and more recently vertical profiles of atmospheric temperature (Fleming, 1978; Smith, 1970; Ulaby, Moore, and Fung, 1981).

Determining the temperature of a portion of the atmosphere from another location in the atmosphere presents problems not encountered in remote sensing of solid surfaces from space. A satellite observing the Earth sees an atmosphere which is monotonically increasing in density along the path of sight. The mixing ratios of many atmospheric constituents are not constant with height but rather are maximums in rather well defined strata. Because each constituent has a spectrally unique radiometric signature this allows a satellite observer to look at just one level or stratum of the atmosphere with minimal radiative contributions from other heights. In this manner a satellite, by observing at several bands in the spectrum, can obtain a vertical distribution of temperatures in the atmosphere (Smith, 1970).

In contrast a horizontal path through the atmosphere encounters very little change in density and almost no variation in concentration of atmospheric constituents. As a result of this homogeneity it is not possible to horizontally remotely sense a portion of the atmosphere at some distance from a radiometer without a significant radiative contribution from the intervening atmosphere. In fact the greatest contribution to the radiance measurement will be from those radiative elements closest to the point of observation, with an exponential attenuation of sensitivity with distance. Since an inference of horizontal temperature gradients requires the radiative measurements of atmospheric elements at some distance from the point of observation, this exponential attenuation requires sophisticated instrumentation capable of discriminating between very similar radiant inputs.

Little work has been done on infrared radiometric horizontal temperature inference and retrieval in the boundary layer and lower troposphere. The most pertinent is that of Peter Kuhn and co-workers (Kuhn, Caracena, and Gillespie, 1977; Kuhn, Nolt and Stearns, 1978; Kuhn and Kurkowski, 1984). Kuhn has exploited the correlation between clear air turbulence and temperature anomalies to develop a radiometric instrument capable of detecting hazardous wind shear environments from several kilometers away.

The next several chapters of this work will examine the infrared radiative properties of the atmosphere and of horizontal temperature gradients. Appropriate band widths and band centers for these measurements will be considered. Two approaches will be examined to infer the temperature gradient magnitude once radiance measurements are obtained. Finally the sensitivity requirements necessary to infer such gradients will be discussed.

Chapter 2

SPECTRAL RADIANCE PROPERTIES OF THE ATMOSPHERE

Before examining the detailed radiation characteristics of the atmosphere it is worthwhile to consider what portion of the infared emission spectrum is best suited to this application. The determination of which portion of the spectrum to use for remote sensing of temperature gradients involves three important factors: signal strength, the sensitivity of the spectral radiance to changes in temperature and IR spectral emission characteristics of the atmosphere. An appropriate spectral band requires a suitable balance of these considerations.

From the instrumental standpoint the greater the optical power coupled into the radiometer the higher the resulting signal to noise ratio (SNR). As the SNR ultimately determines the accuracy of an individual measurement, it is desirable to keep this parameter large. Three factors determine the input signal strength from a given radiant source: the emitting properties of the source, the amplitude of the Planck function Eq (1.1) and the bandpass characteristics of the radiometer. From Figure 2.1 it can be seen that the Planck function varies by several orders of magnitude for wavenumbers between 1 cm^{-1} and 4000 cm^{-1}. The wavenumber of maximum intensity, ν_{max} is given by Wien's displacement law

$$\nu_{max}(T) = \alpha T \tag{2.1}$$

where $\alpha = 1.9610\ \mathrm{cm}^{-1}\ {}^{\circ}K^{-1}$. For a typical boundary layer temperature of 20° C ν_{max} is 575 cm^{-1}. The bandpass is determined by the transfer function $t(\nu)$, in general a complicated relationship determined by the physical characteristics of the instrument.

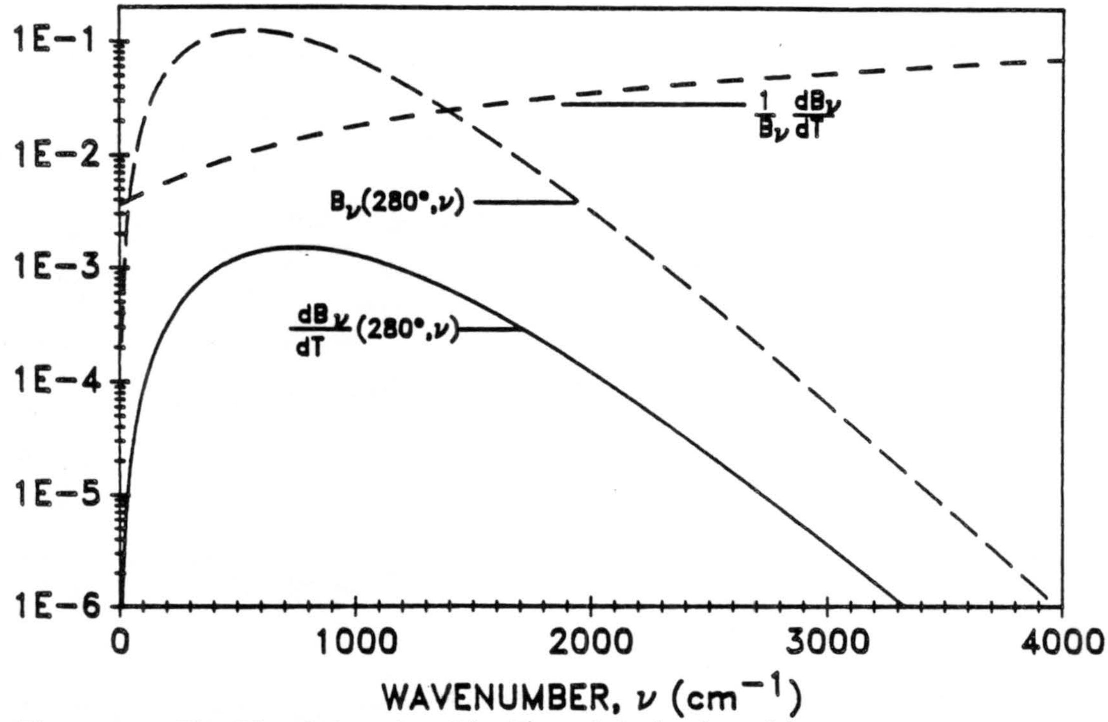

Figure 2.1: *The Planck function $B(\nu,T)$ and derivative with respect to temperature*

It is common to further limit the bandpass with the use of filters permitting a single instrument to measure several smaller discrete bands. In this case the transfer function takes the form $t(\nu) = \tau(\nu)F(\nu)$, F being the filter transfer function and τ, the instrument transfer function. F(ν) tends to be relatively peaked in comparison to the instrument transfer function. The input signal measured by the radiometer is

$$S(T,\tau) = \int_0^\infty \varepsilon(\nu,T)B(\nu,T)\tau(\nu)F(\nu)d\nu. \tag{2.2}$$

The spectral emissivity, ε is defined by the relationship $R(\nu,T) = \varepsilon(\nu,T)B(\nu,T)$ where $R(\nu,T)$ is the actual radiance. The emissivity is bounded from above by unity with a minimum value of 0. Since Eq. (2.2) involves an integral over the Planck function it is apparent that a broad filter function yields a larger intensity than a narrow filter function. For reasons to be discussed later however it may be desirable to sacrifice signal strength for increased spectral resolution.

The second major consideration is the sensitivity of the radiance to changes in temperature. The relative change per degree for a blackbody is given by:

$$\delta R(\nu,T) = \frac{1}{B(\nu,T)}\frac{\partial B}{\partial T} = \frac{C_2\nu/T^2}{1-e^{\frac{-C_2\nu}{T}}} \tag{2.3}$$

that is, the derivative of the Planck function with respect to temperature divided by the Planck function. For terrestrial temperatures Eq (2.3) $\approx \frac{C_2\nu}{T^2}$. In the limit that $\nu \rightarrow 0$ Eq. (2.3) $\rightarrow T^{-1}$. A portion of Eq. (2.3) is plotted in Figure 2.1. By inspection it is obvious that for the temperature range seen in the boundary layer Eq. (2.3) increases monotonically with increasing ν. Note however that the Planckian intensity decreases rapidly for $\nu > \nu_{max}$ and even though the radiant sensitivity increases with ν the intensity quickly becomes too small for accurate measurement.

Since equation (2.3) is relatively slow-changing in the region of the spectrum where the Planck function is near its maximum, this region would seem a likely candidate for temperature gradient sensing if atmospheric emission characteristics are suitable.

The spectral emission characteristics of the atmospheric boundary layer are the third major consideration in spectral band selection. Kirchoff's law states that for an atmosphere in local thermodynamic equilibrium the spectral absorption α_ν of an atmospheric element is equal to the spectral emissivity ε_ν of that element. As a result of Kirchoff's law and the radiative variability in the atmosphere there are spectral regions where the atmosphere is almost transparent and other regions where it becomes almost opaque over a distance of a few meters. For the purpose of measuring temperature gradients over a few kilometers a portion of the spectrum between the above two limits is required.

Unlike solids which emit more or less continuously over the spectrum, emission spectra of many atmospheric gases consist of a great number of characteristic lines, often very closely spaced. This is a natural outcome of the fact that the quantum mechanics permits only certain discrete transitions between energy states of atoms and molecules. These transitions can be between differing electronic energy states or between different vibrational and rotational states. The energies associated with these transitions depend on the structure of the particular molecular species. Furthermore the probability of transition, and hence the line strength, varies greatly across the spectrum.

Because of the wide variety of possible combinations of transitions and interactions even simple molecules exhibit rich and very complex line spectra. As a result of such a detailed structure the emission from a particular atmospheric constituent can vary widely even in a very narrow portion of the IR spectrum. The atmosphere is composed of several such gases each with its own emission spectrum. The atmosphere as a whole has a spectrum which is, to first approximation, a product of the individual spectra. Such a composite spectrum is of course a function of the mixing ratios of the constituent gases and hence can vary widely as mixing ratios change.

As seen from Eq. (2.1) the portion of the spectrum from 500 cm^{-1} to 600 cm^{-1} is, for terrestrial temperatures, the region of maximum radiant power density as given by the Plånck function. The two predominant emitting gases in this region are H_2O with typical mixing ratio values ranging from less than 2 g/kg to more than 30 g/kg and CO_2 with a typical mixing ratio value of about .5 g/kg. Though ozone has a strong fundamental band centered at about 700 cm^{-1} and is important in the stratosphere, it is negligible in the boundary layer because of its small concentration there.

The linear and symmetric CO_2 molecule is one of the most studied molecules from the spectroscopic standpoint, both theoretically (Herzberg, 1943) and experimentally (Burch, Gryvnak and Patty, 1966; Madden, 1961). The most important feature of CO_2 in the 400 cm^{-1} to 800 cm^{-1} band is the existance of the vibratory fundamental ν_2 centered at around 667 cm^{-1}. For each vibrational state there exist many different rotational states. Since energy transitions between vibrational states occur simultaneously with transitions between rotational states there are a number of discrete spectral lines associated with a given vibrational transition. As the rotational transitions are of a much lower energy than their vibrational counterparts, these discrete lines are relatively closely clustered giving a vibrational band.

Goody (1964) notes that in addition to the fundamental ν_2 transition there exist 14 overtone and combination bands with a total intensity of about 10 percent of the fundamental. Several isotopes of CO_2 also exist in the atmosphere in minor amounts. These isotopes have bond strengths and moments of inertia differing slightly from the ubiquitous $C^{12}O_2^{16}$. Most of these isotopes also lack the symmetry of $C^{12}O_2^{16}$. These differences give rise to energy levels slightly perturbed from those of common CO_2. In fact Stull, Wyatt and Plass (1963) consider over 1800 vibrational/rotational transitions when computing the high resolution CO_2 spectrum numerically..

In contrast to the relatively well ordered and periodic CO_2 spectrum the water vapor spectrum is seemingly random in the 500 cm^{-1} to 800 cm^{-1} regime. The least energetic vibrational fundamental is centered at 1595 cm^{-1}, well out of the area of interest. As the H_2O molecule has no 3– fold axis of symmetry it is of the "asymmetric top" variety with differing principal moments of inertia. The large permanent dipole moment of the H_2O molecule causes the rotational bands to be quite intense with strong absorption even in the far wings. Indeed Kondrat'ev (1973) notes that the band centered at 200 cm^{-1} is responsible for the absorption observed in the 500 cm^{-1} to 800 cm^{-1} region. As with CO_2, water vapor has several isotopes whose mixing ratios compared with that of common H_2O vary with season and location. In addition other researchers (Bignel, 1969; Cox, 1969; Cox, 1973; Idso, 1980) have found that dimers (pairs of H_2O molecules linked with weak hydrogen bonds) are present in sufficient concentrations to create significant differences between theory and measurement.

It is important to note that the mixing ratio of water vapor in the boundary layer can range from 2 to 75 times that of CO_2. As a result of this disparity even relatively weak lines in the H_2O emission spectrum can dominate similarly located intense lines in the CO_2 spectrum (Wang and Ryan, 1982). Because of the large and variable amounts of atmospheric water vapor the composite atmospheric emission spectrum which includes the emissions of both major substances shows a marked dependence on the ambient H_2O mixing ratio. Only in those regions where CO_2 dominates, as in the 600 cm^{-1} to 700 cm^{-1} band, is there little water vapor concentration sensitivity.

Figure 2.2 is a plot of the ratio of CO_2 transmittance to H_2O transmittance through 5 kilometers of atmosphere as a function of wavenumber. Two curves are shown; the upper for an H_2O mixing ratio of 5 g/kg (30 percent relative humidity) and the lower for a mixing ratio of 15 g/kg (saturated air). These curves represent two quite different humidity

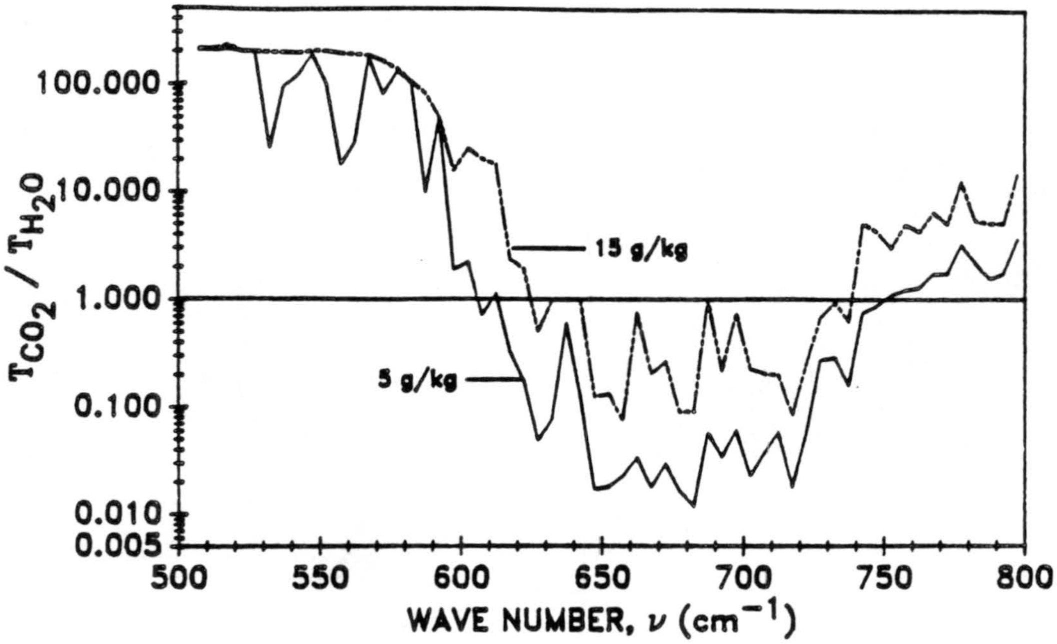

Figure 2.2: *The ratio of carbon dioxide spectral transmittance to water vapor spectral transmittance for 2 water vapor mixing ratios*

conditions frequently encountered in the summer boundary layer. For both situations H_2O absorption far exceeds that of CO_2 for wavenumbers below about 600 cm^{-1}. From about 650 cm^{-1} to 725 cm^{-1} CO_2 dominates the absorption, with the exception of a few strong H_2O rotation lines. From 725 cm^{-1} to 800 cm^{-1} H_2O shows increasing domination.

From comparisons between the two curves one can note regions such as around 560 cm^{-1}, 615 cm^{-1} and from 650 to 720 cm^{-1} where the transmittance ratios vary by an order of magnitude or more. In contrast there are other regions where the ratio is much less sensitive to changes in H_2O mixing ratio. This occurs where H_2O absorption dominates that of CO_2 i.e. where $\frac{T_{CO_2}}{T_{H_2O}} > 1$.

Figure 2.3 illustrates the total transmittance $T_{tot} = T_{CO_2} \times T_{H_2O}$ in this range. The total transmittance is plotted for the two mixing ratio cases above. The strong CO_2 absorption in the 600 to 700 cm^{-1} region gives very small transmittance values. For $\nu > 750 cm^{-1}$ the transmittance is still several percent and strongly dependent on H_2O mixing ratio values as can be seen by the separation of curves. In the region from 500 cm^{-1} to 600 cm^{-1} there are narrow bands centered at 535 cm^{-1}, 560 cm^{-1} and 585 cm^{-1}

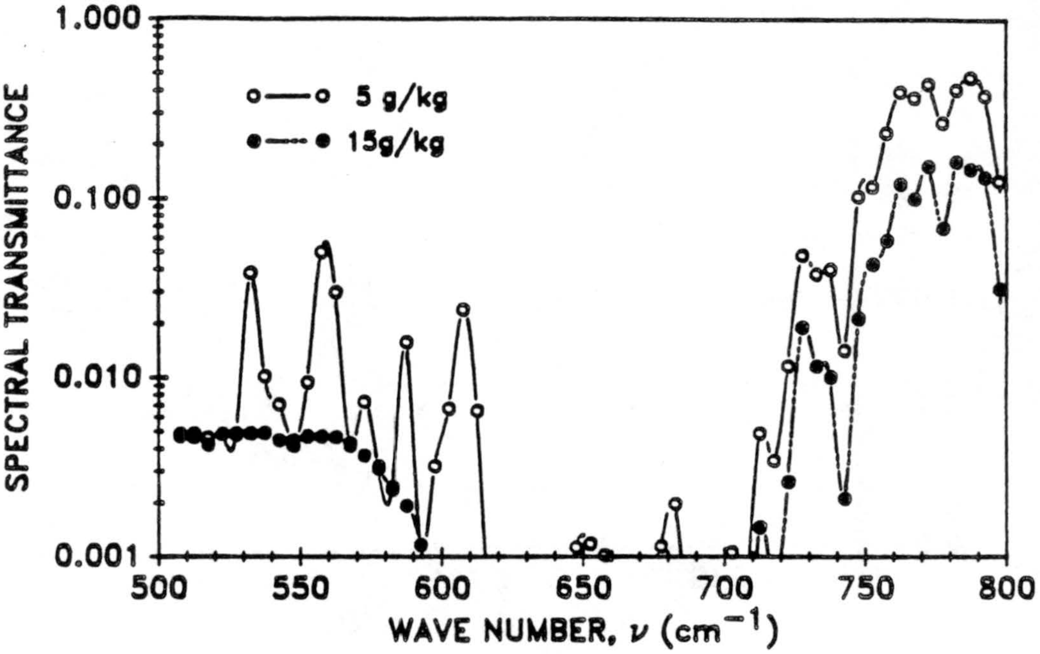

Figure 2.3: *Spectral transmittance vs. wavenumber for two water vapor mixing ratios*

where the transmittance is strongly mixing ratio dependent and bands centered at 550 cm^{-1}, 570 cm^{-1} and 580 cm^{-1} where little or no H_2O mixing ratio dependency exists.

From the above discussion it should be clear that there is no single band which would be universally appropriate for temperature gradient sensing. To a large extent the scale of the gradient to be measured determines the spectral band to use. For a large scale, small magnitude gradient a relatively transparent spectral region would yield the best result. Conversely for a gradient of small extent but large magnitude a relatively more opaque spectral bandpass is better since in this case the atmosphere warms or cools more quickly with increasing path length. Another situation where rapid attenuation may be desirable is that in which solar heated solid objects, such as canyon or valley walls exist in the far field of the path of observation. Only a 2% contribution from such a surface can significantly contaminate temperature gradient measurements if the surface temperature T_s varies significantly from the ambient air temperature. In this case the best band choice would have enough attenuation to make the heated surface contribution negligible.

The water vapor mixing ratio sensitivity is an important factor in any situation where the mixing ratio may vary over the region of measurement, for example in the outflows of convective systems (Kuhn and Kurkowski, 1984). In such cases it is desirable to use a portion of the spectrum which has little humidity dependence. In situations where temperature gradients are driven by surface heating and the surface is dry, humidity gradients would not be expected to be significant.

A final consideration is the appropriate selection of band width. As noted by Kuhn and Kurkowski (1980), " Theoretical considerations show that narrow passbands give the best spatial discrimination of thermal perturbations, while broad pass bands produce the strongest signal ". For optimum spatial resolution it is necessary to have the mass absorption coeffecient $k(\nu)$ as constant as possible across the passband. As was seen in Figure 2.3 the transmittance (and hence $k(\nu)$) varies considerably over just a few wavenumbers. Because of this rapid variation a narrow pass band offers higher resolution. Signal strength is however linearly dependent on band width over small intervals, and the trade-off for small band width and high resolution is a corresponding decrease in signal strength. A reasonable compromise for many radiometers is a band width of about 5 to 15 cm^{-1}. The work described herein is done using a 5 cm^{-1} bandwidth but may generalized to a larger values of $\Delta\nu$.

Chapter 3

A NUMERICAL MODEL FOR CALCULATING IR RADIANCES

The effect horizontal temperature gradients have on the IR radiance is best determined by actual measurements in a laboratory situation. As is the case with many large scale natural phenomena this ideal control over conditions is impossible to realize. The most practical method of study is by means of numerical simulation. This chapter discusses the numerical model used in this work to simulate the radiative effects a temperature gradient has on the background or basic state radiation field.

To find the radiance $R(\nu, T, \phi)$ the integral form of the radiative transfer equation

$$R(\nu,T) = \underbrace{\int_0^{\varepsilon'} B(\nu,T)d\varepsilon}_{a} + \underbrace{(1-\varepsilon')\varepsilon_{sfc}B(\nu,T_s)}_{b} \tag{3.1}$$

must be solved. The integral in term a is the atmospheric contribution to the radiance. Term b is the boundary or surface term which in this application may be a canyon wall, mountain side, or perhaps even an optically thick cloud, T_s being the temperature of such a surface and ε_{sfc} the surface emissivity. As mentioned in the previous chapter it is desirable to minimize the contribution from term b such that it is negligible. In this case ε' can be set equal to unity and term b can be dropped. The radiative transfer equation then becomes

$$R(\nu,T,\phi) = \int_0^1 B(\nu,T)d\varepsilon \; . \tag{3.2}$$

Note that Eq. (3.2) is valid only for a single wavenumber. Since any physically realizeable radiometer measures over some finite wavenumber interval, calculating the radiance measured by such an instrument requires Eq (3.2) itself to be integrated over a finite range of wavenumbers. The optical power measured by the radiometer also increases as the measured portion of the radiation spectrum increases, a desirable condition from the standpoint of instrument signal to noise ratio.

The transmittance even for a single wavenumber is a complex function of pressure, temperature and mixing ratios of the constituent emitting gases and hence is in general not expressible in exact analytical form. Instead the transmittance is approximated in some manner, usually as the average over some finite wavenumber interval. This usually means that it is not possible to solve equation (3.2) exactly, rather it must be approximated numerically.

The radiative transfer model used in this work incorporates a transmission calculation scheme developed by W. L. Smith (1969). Smith statistically fit calculated transmission data for the rotational H_2O band and for the 15 micron CO_2 band (Stull, Wyatt, and Plass, 1964) to a polynomial in powers of temperature, pressure, and individual mixing ratios. Out of the 24 terms in powers of temperature, pressure and optical mass considered, it was found that an eight term polynomial was sufficient to approximate the calculated data over 5 inverse cm. intervals to within 1% RMS over most of the spectrum considered. This method allows for a fair degree of spectral resolution in rapid transmission calculations over the range of pressures and temperatures typically found in the atmosphere. As noted by Smith the method agrees fairly well with experimentally derived transmission measurements and balloon-borne measurements in the real atmosphere.

To approximate Eq. (3.2) numerically the integral is converted to a sum and the differential in emissivity $d\varepsilon$ is converted to a finite difference in transmittance $\Delta\tau$ assuming thermal equilibrium and no scattering which implies $\tau_\nu + \varepsilon_\nu = 1$. Except in computing the transmittance the average values of temperature and pressure in the particular finite radiating element are used in the calculation of each element in the sum. Since the transmission involves all the finite elements between the observer and the radiating element it is necessary to use the cumulative mass-weighted average temperature and pressure

$$p_{eff} = \frac{\int_0^U p\, dU'}{\int_0^U dU'} \qquad T_{eff} = \frac{\int_0^U T\, dU'}{\int_0^U dU'} \tag{3.3}$$

in this part of the calculation. With these changes the finite form of Eq (3.2) becomes

$$R(\nu,T) = (-)\sum B(\nu,\bar{T})\Delta\tau(T_{eff},p_{eff}) \tag{3.4}$$

where the overbar implies an mean value for the finite radiating element. The minus sign in (3.4) arises from the fact that $\Delta\tau$ is negative since transmission decreases along the path.

To calculate the total cumulative transmission at each step the individual transmissions, τ_{CO_2} and τ_{H_2O} are calculated separately and then multiplied to provide the actual transmission: $\tau_{total} = \tau_{CO_2} \times \tau_{H_2O}$ as done by Smith. (This is not strictly valid due to the neglect of the overlap, which essentially allows a single photon to be absorbed by both gases. However it is fairly accurate for the small wavenumber intervals considered here.) The difference between this transmittance and the previous value is, by Kirchoff's law and the assumption of local thermodynamic equilibrium, the finite difference in emissivity and hence the weighting value for the radiance from the particular element being considered.

Though the bounds on the sum in Eq. (3.4) are from a transmittance of unity to a transmittance of zero the corresponding sum in the model is terminated when $\tau_{total} \leq .01$. This is done because in some instances the transmission calculation scheme becomes unstable for very small values of τ. The sum is then divided by $1 - \tau_{total}$ to correct for the truncation. The spatial resolution of this model is 20 meters. It is assumed that in the limit of very small spatial resolution the sum (3.4) converges to Eq. (3.2).

Though the model incorporates effects due the earth's curvature this was found to be unimportant in most cases. The correction to the elevation of a point lying on the line of sight at a distance x from the observer is given by

$$\delta z = \sqrt{a^2 + x^2} - a \simeq x^2/2a \tag{3.5}$$

where a is the radius of the earth. At a point 10 km. from the observer the curvature correction is about 8 meters and at 20 km. only about 30 meters. Assuming the worst case, a dry adiabatic lapse rate $\Gamma_d = 9.8°K/km$, this gives temperature corrections of $-.08°$ and $-.30°$ for 10 km. and 20 km. respectively. Due to the quadratic relationship in

Eq. (3.5) this correction grows rapidly for large x, but in this application look distances seldom exceed 20 km. Curvature effects could be important in situations where a shallow temperature inversion exists. In this case it might be possible for the Earth's curvature to allow the observer to see the warm air capping the inversion at distances far from the point of measurement. In such situations use of a spectral band with rapid attenuation and short range would be warranted.

The calculations made using the model produce radiance values. Any real radiometer will actually measure an irradiance, which is the radiance integrated over whatever solid angle the instrument optics accept. As shown in the previous paragraph the vertical temperature change with height gives rise to vertical temperature gradients far in excess of those seen in the horizontal. While a half angle of acceptance of less than 3 milliradians (.17 degrees) is frequently achievable this still represents a finite solid angle over which the temperature will vary. Also to avoid spurious radiance contributions from the ground the actual zenith angle seen by the radiometer must be somewhat less than the 90° zenith angle on which the calculations are based. However radiance calculations made for zenith angles within a few degrees of 90° show very little variation from the horizontal case. Hence a finite acceptance angle should result in only a very slight departure when comparing actual measurements with computed values, assuming the angle is kept suitably small.

In making the radiance calculations several implicit assumptions are made in addition to the condition of local thermodynamic equilibrium. With the exception of the imposed horizontal temperature gradient and the density variation to which it gives rise, the atmosphere is considered to be horizontally uniform. Scattering is assumed to be negligible, a fair assumption in the IR portion of the spectrum for a reasonably non-turbid cloudless atmosphere. Surface pressure is assumed to be constant. Radiances are considered Planckian and radiance contributions from substances other than CO_2 and water vapor are considered negligible in the portion of the spectrum considered here. As frequently done (*ex.* Wark, 1961) mixing ratios of CO_2 are assumed constant throughout the troposphere. While this is sound with respect to CO_2 one must use caution in applying this to H_2O, a highly variable atmospheric constituent in both space and time. Unless otherwise stated these assumptions are used in all radiance calculations described in this work.

Chapter 4

RADIANCE CHARACTERISTICS OF HORIZONTAL TEMPERATURE GRADIENTS

The purpose of this chapter is to examine the sensitivity of the radiance to temperature gradients. As with all experiments described in this work a cloudless homogeneous atmosphere with surface temperature T_o is assumed. On this basic state atmosphere a constant temperature gradient perturbation of magnitude ∇T is imposed as shown in Figure 4.1. This gives

$$T(\vec{x}) = T_o + \vec{x} \cdot \vec{\nabla} T. \tag{4.1}$$

Using this perturbed atmosphere radiances were calculated at different values of the azimuth angle ϕ with $\phi = 0°$ being the radiance measured looking up the gradient toward higher temperatures. R($\phi = 90°$), the radiance measured orthogonal to the gradient, is independent of gradient magnitude since T = const. on this path. After the radiances are calculated for the domain $0° \leq \phi \leq 180°$. normalized radiances N(ϕ) are calculated.

The normalized radiance is given by

$$N(\phi) = \frac{R(\phi)}{R(90°)} \, . \tag{4.2}$$

In this manner the radiances are scaled to the cross gradient value. This normalization or scaling has a number of advantages. N(0°) (or N(180°)) gives the percentage difference a radiometer must resolve in order to detect a gradient of magnitude ∇T. Also, assuming that the signal output of the radiometer is proportional to the measured radiance, N(ϕ) is independent of the constant of proportionality. This removes many of the calibration problems associated with radiometric measurements.

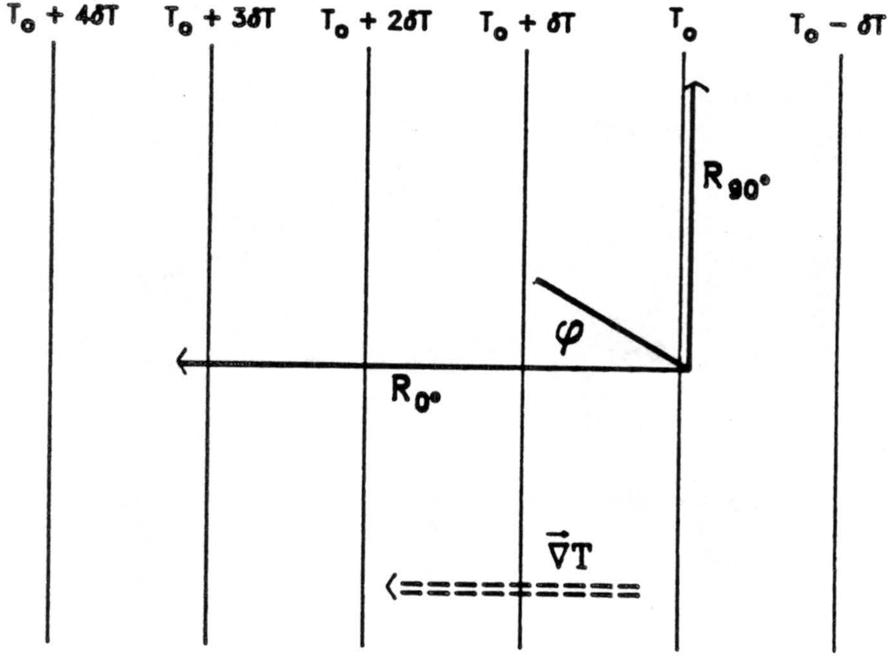

Figure 4.1: *Schematic diagram of the experimental layout.*

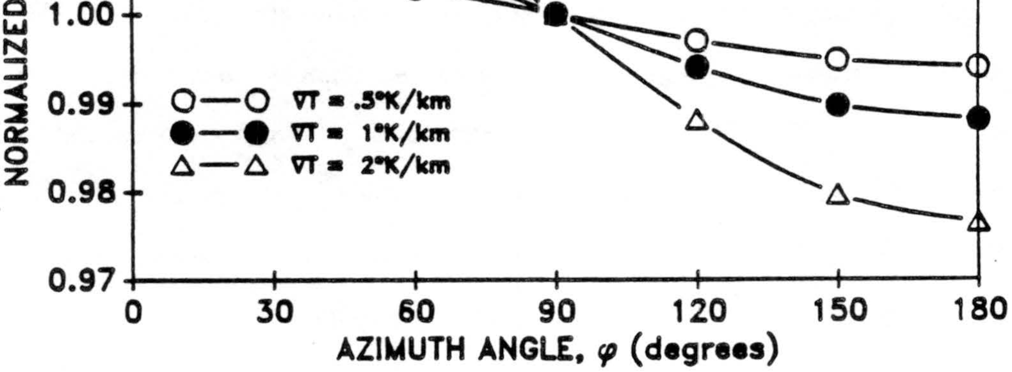

Figure 4.2: *Normalized radiance vs. azimuth angle for three temperature gradient magnitudes.*

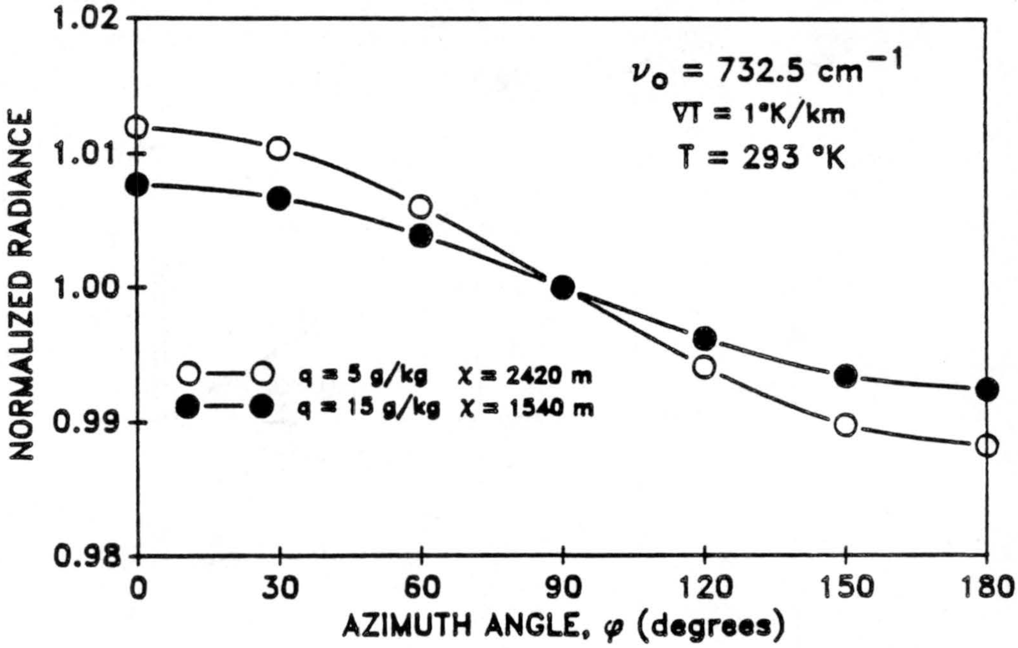

Figure 4.3: *Normalized radiance vs. azimuth angle for two water vapor mixing ratios.*

Figure 4.2 shows N(ϕ) for several values of gradient magnitude. The bandwidth is 5 cm^{-1} centered on $\nu_o = 732.5\ cm^{-1}$. As the gradient increases the amplitude of N(ϕ) increases in an approximately linear manner. Also the N(ϕ) curves appear to be symmetric about the point $\phi = 90°$, the nongradient value.

The attenuation length χ is a convenient parameter to use in comparing the behavior of N(ϕ) as ν_o changes. The attenuation length is defined as that distance where the spectral transmittance is equal to e^{-2}, i.e. the transmittance e squared folding length. Figure 4.3 compares two curves of N(ϕ) for the same atmosphere with the exception of humidity content. The higher amplitude curve, which is the same as that shown in Fig. 4.2 for $\nabla T = 1°$ K/km has a mixing ratio of 5 g/kg and a corresponding attenuation length of 2420 m. The curve with lesser amplitude is for a mixing ratio of 15 g/kg and $\chi = 1540$ m. The values of N(0°) are about 1.008 and 1.012 for $\chi = 1540$ m and $\chi = 2420$ m respectively. This would indicate that a radiometer would need to be sensitive to about a 1% change in radiance with this $\Delta\nu$ and ν_o to be able to detect the gradient and a much greater sensitivity to accurately diagnose the magnitude of the gradient.

Another important concept is that of the brightness or effective radiative temperature, T_B. This is the temperature of a black body radiator which produces the same radiance as is measured by a radiometer and is given by

$$T_B = C_2\nu(\ln(\frac{C_1\nu^3}{R_\nu} + 1))^{-1}. \tag{4.3}$$

Equation (4.3) is found by solving Planck's law, Eq. (1.1) for the temperature. Using the brightness temperature the normalized radiance N(ϕ) can be expressed as

$$N(\phi) = \frac{e^{\frac{C_2\nu}{T_o}} - 1}{e^{\frac{C_2\nu}{T_B(\phi)}} - 1} \tag{4.4}$$

where $T_B(\phi)$ is the brightness temperature corresponding to the radiance R(ϕ). For the ranges of temperature and wavenumber being considered here Eq. (4.4) can be approximated as

$$N(\phi) \simeq e^{\frac{C_2\nu\delta T}{T_o^2}} \tag{4.5}$$

where $\delta T = T_B - T_o$. Solving Eq. (4.5) for δT gives

$$\delta T = \frac{T_o^2}{C_2\nu} \ln N(\phi, \nabla T) \ . \tag{4.6}$$

Equation (4.6) expresses the temperature sensitivity a radiometer must have to resolve the temperature gradient which gives rise to N($\phi, \nabla T$). For the 2 cases in Fig. 4.3 $\delta T = .65°$ for $\chi = 1540m$ and $\delta T = .97°$ for $\chi = 2420m$.

The large difference in χ values in Figure 4.3 points out the sensitivity of the technique to changes in water vapor content. An examination of Figure 2.1 shows that the band center $\nu_o = 732.5\ cm^{-1}$ is in a region where there is comparatively little difference between the 5 g/kg and 15 g/kg curves. Also for both of these curves $\frac{T_{CO_2}}{T_{H_2O}} < 1$ indicating that even for the larger mixing ratio value CO_2 is the dominating absorber.

To increase N(0°) for the case of the 15 g/kg mixing ratio a different wave number band must be chosen. Figure 4.4 shows plots of N(ϕ) for the same two atmospheric conditions as Fig. 4.2. Here however the radiance for the more moist case was measured

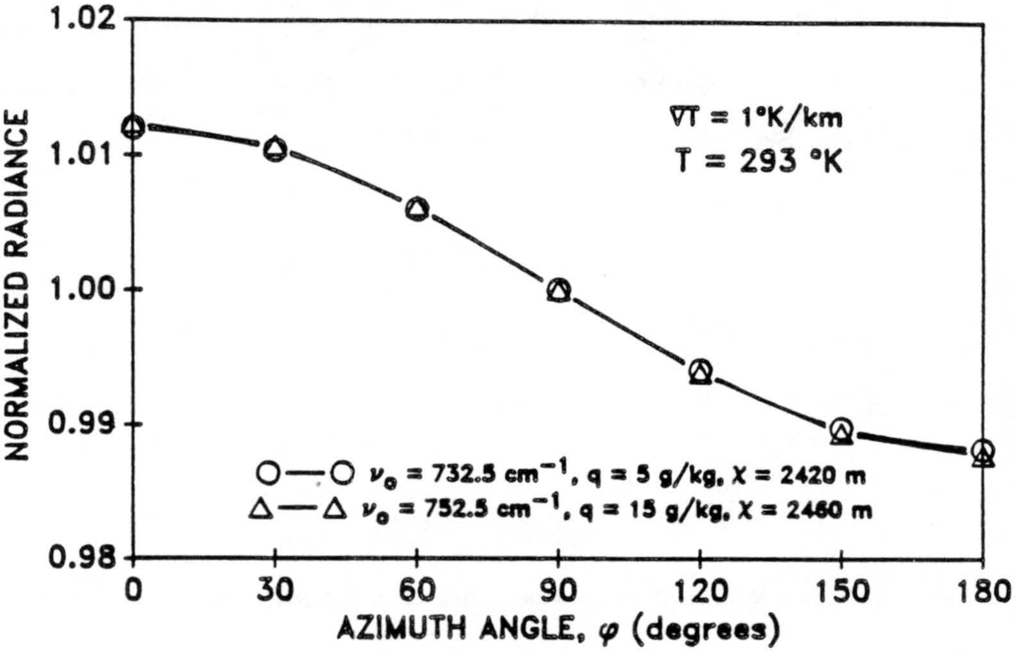

Figure 4.4: *Normalized radiance vs. azimuth angle for two differing water vapor mixing ratios and wavenumbers but similar attenuation lengths.*

at $\nu_o = 752.5\,cm^{-1}$. The attenuation length for the moist atmosphere at 752.5 cm^{-1} is 2460 m, only 40 m different than the 732.5 cm^{-1} attenuation length in the dry atmosphere. Fig. 4.4 shows excellent agreement between the two simulated measurements and demonstrates the utility of the attenuation length in characterizing the spectral radiance in differing atmospheres.

In Figure 4.5 attenuation lengths for both atmospheres are plotted as a function of wave number. Attenuation length water vapor dependency again varies considerably across the spectrum, being least sensitive near the center of the CO_2 absorption bands. The largest disparity between the curves is in the large wave number extreme where water vapor absorption dominates and the atmosphere is most transparent.

Although the attenuation length is a useful quantity it should be noted that there is not a one-to-one relationship between normalized radiance and attenuation length for specified atmospheric conditions. This is condition arises for two reasons. The normalized radiance has a slight dependency on wavenumber as will be demonstrated later. More fundamental however is the functional dependence of transmittance on optical mass and hence

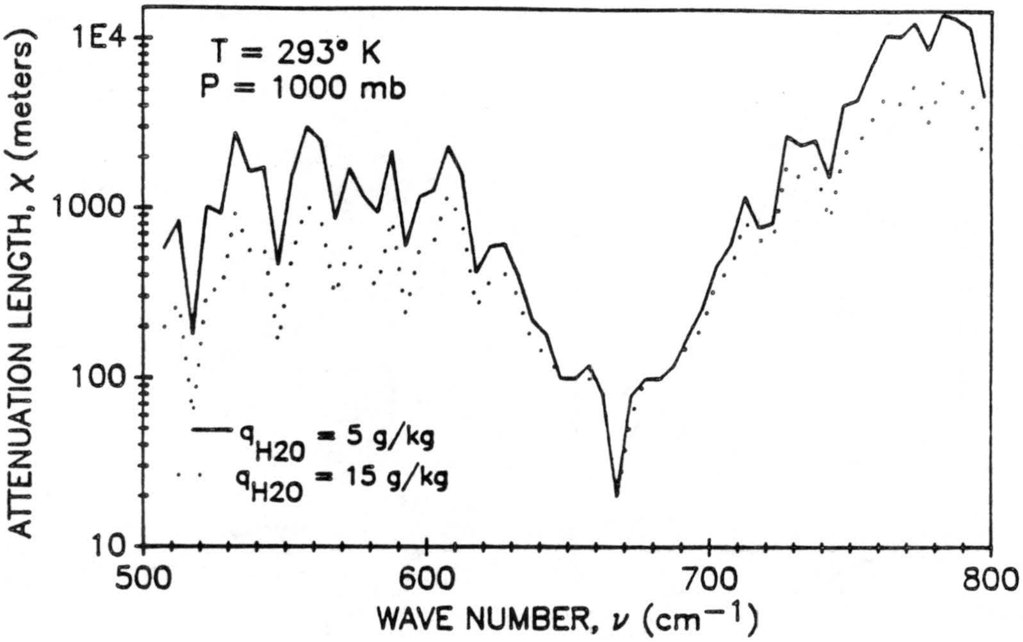

Figure 4.5: *Attenuation length χ vs. wavenumber for two water vapor mixing ratios.*

geometric distance. Often in transmittance calculations a mass absorption coeffecient, k_ν is assumed and in the case of a nonscattering medium a Beer's law (exponential) relationship is used. In the case of transmittance through a homogenous gas this relationship becomes

$$\tau_{Beer} = e^{-q\rho k_\nu x} \tag{4.7}$$

where q is the mixing ratio of the emitting gas, ρ the atmospheric density and x is geometric distance. When Eq. (4.7) holds there is a simple relationship between χ and k_ν; $q\rho k_\nu \chi = 2$, and choosing a χ value specifies a unique value for k_ν. While Eq. (4.7) is valid for a single emitting line it becomes less accurate as the wavenumber bandpass becomes larger. Though this strategy of assuming an exponential relationship for a larger spectral bandpass has been exploited successfully in several circumstances, it is not satisfactory for this work.

Figure 4.6 shows a plot of transmittance vs. distance for two almost identical attenuation lengths calculated from Smith's coefficients. Also shown is a transmittance calculation made assuming Beer's law and an attenuation length the mean of the other

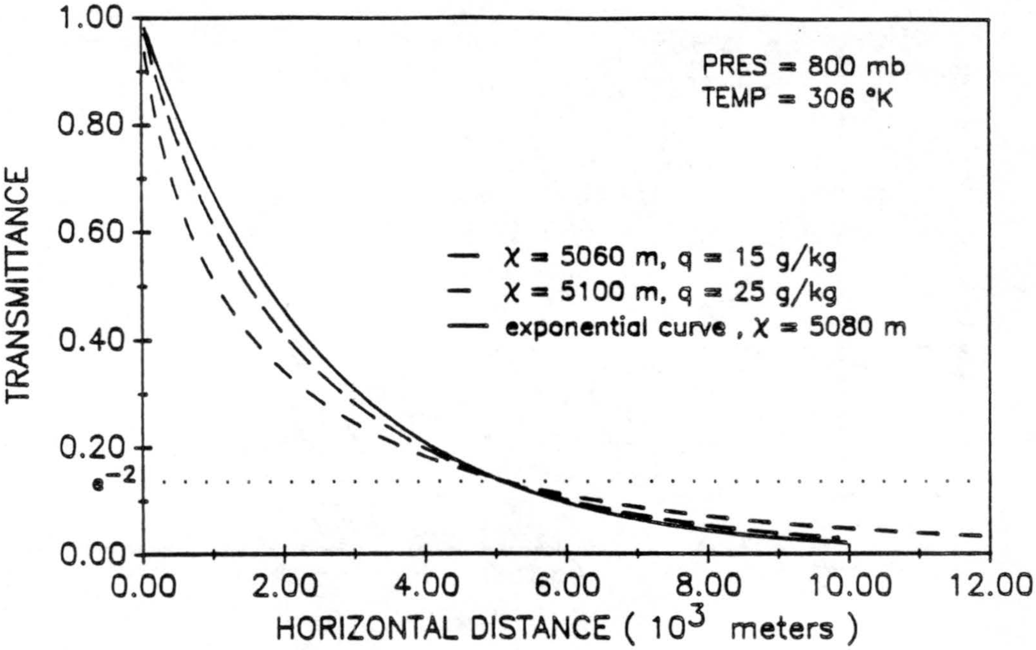

Figure 4.6: *Transmittance vs. geometric distance for two examples of Smith's transmittance scheme contrasted with exponential attenuation of Beer's law.*

two cases. While the all three intersect at (almost) the same point there are notable differences between each of the curves. Rewriting Eq. (3.4), the finite difference radiative transfer equation, as

$$R(\nu,T) = (-)\sum B(\nu,\bar{T})\frac{\Delta\tau}{\Delta x}\Delta x \tag{4.8}$$

it is apparent that the weighting factor $\frac{\Delta\tau}{\Delta x}$ for each element is the (average) slope of the τ vs. x curve for that element. Inspection of Fig. 4.6 reveals that $\frac{d\tau}{dx}$ varies from one curve to the next, especially for $x \leq \chi$. The initially steeper slope of the Smith transmittances weights the closest elements more heavily than does the exponential curve. Since these elements are not far enough down the gradient to have a temperature much different from T_o, normalized radiances calculated using Smith's method are smaller than N(ϕ) calculated using Beer's Law. This also explains why the same attenuation length and physical conditions can yield different normalized radiances for different passbands. Though this example from the Smith method is much more extreme than usually encountered, it is demonstrative of the variability seen in observations. As H_2O mixing ratios increase, the disparity between normalized radiances with similar attenuation lengths decreases.

From the foregoing discussion it is evident that no single wave number band is appropriate for temperature gradient sensing. The band center instead must be chosen to best fit the ambient density and water vapor content. Other important criteria for band choice are geometric extent of the gradient and gradient magnitude. As noted before the amplitude of oscillation of $N(\phi)$ is a function of attenuation length, the greater the attenuation length the larger the amplitude. It may be desirable to choose a larger χ for measuring a weak gradient. The geometric extent of the gradient however puts an upper limit on the size of χ as the radiometer should not see beyond the gradient boundary.

Chapter 5

SPECTRAL BEHAVIOR OF THE NORMALIZED RADIANCE

In the last chapter the normalized radiance was introduced as a way of comparing radiances at arbitrary azimuth angles with the radiance measured perpendicular to the gradient (or equivalently with the radiance value if no gradient were present). The normalized radiance is still a function of wavenumber although it is much less sensitive to wavenumber variations than the non-normalized radiance, $R(\phi)$. In this chapter the wavenumber dependence of $N(\phi)$ is examined and two methods are developed to compensate for this dependence.

To understand the spectral behavior of the normalized radiance the following numerical experiment was performed. A set of transmittance vs. distance data points with an attenuation length of 7060 meters was generated using Smith's method. Using this transmittance data in Eq. (4.8), normalized radiances were calculated for a fixed base state temperature and $500cm^{-1} \leq \nu \leq 800cm^{-1}$, the only degree of freedom being the wavenumber. This $N(\nu)$ curve is shown in Figure 5.1. Also shown in Fig. 5.1 is the brightness temperature, $T_B(\nu)$, found using Eq. (4.3) and $R(\nu, \phi = 0)$. $N(\nu)$ varies almost linearily by about 1.7% across the domain of ν while T_B is essentially constant varying by only .012%, less than $.03°K$.

From the linearity of $N(\nu)$ it is reasonable to assume that N can be approximated quite adequately by the truncated Taylor series

$$\tilde{N}(\nu) = N(\nu_o, T_o, T_B) + \left[\frac{\partial N}{\partial \nu}\right]_{\nu_o, T_o, T_B} (\nu - \nu_o) \tag{5.1}$$

where

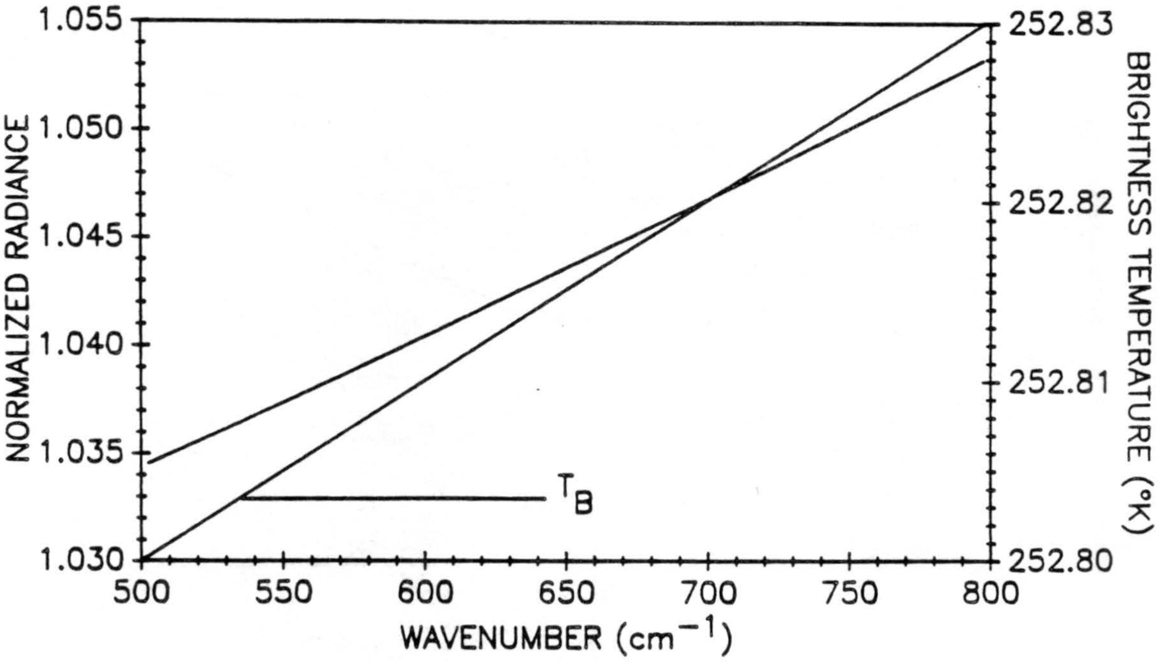

Figure 5.1: ***Normalized radiance and brightness temperature T_B vs. wavenumber for a constant attenuation length.***

$$\frac{\partial N}{\partial \nu} = C_2 \frac{(1/T_o - 1/T_B)e^{C_2\nu(1/T_o+1/T_B)} - e^{C_2\nu/T_o}/T_o + e^{C_2\nu/T_B}/T_B}{(e^{C_2\nu/T_B} - 1)^2}$$

$$\simeq \frac{C_2 \delta T}{T_o} e^{c_2 \delta T \nu / T_o}. \tag{5.2}$$

The approximate form, which comes from differentiation of Eq. (4.5) shows clearly why N increases with increasing ν as seen in Fig. 5.2. Also shown is the approximated $\tilde{N}(\nu)$ (long dashed line) indicating very good agreement.

By rearranging Eq. (5.1) it is possible to define a centered normalized radiance

$$N_c(T_o, T_B) = N(\nu, T_o, T_B) - \left[\frac{\partial N}{\partial \nu}\right]_{\nu_o = 650cm^{-1}, T_o, T_B} (\nu - 650cm^{-1}) \; . \tag{5.3}$$

N_c is <u>not</u> a function of ν but is rather the normalized radiance for the given T_B which would be measured at the center of the wavenumber spectrum of interest, 650 cm^{-1}. Further, once the temperature gradient and base state temperature T_o are specified the attenuation length is determined. In this manner N_c can be considered a function of χ.

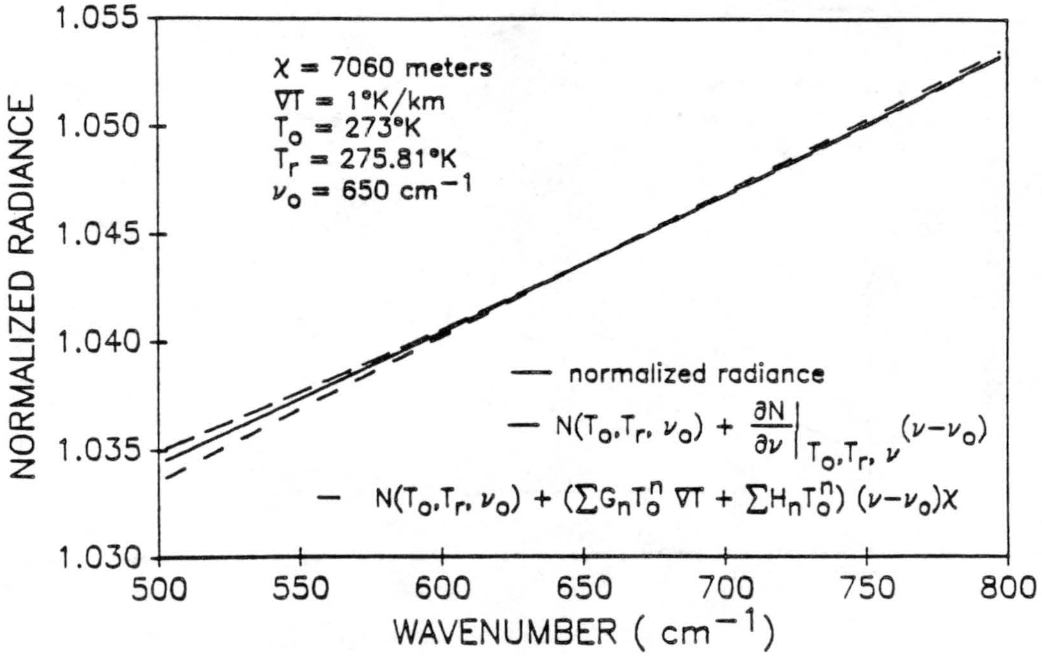

Figure 5.2: *Normalized radiance and two approximate forms of normalized radiance vs. wavenumber.*

While Eq. (5.3) provides an accurate method of finding a centered normalized radiance, it is limited in practice by the requirement of exact calibration of the radiometric instrument to determine the brightness temperature. One of the advantages of using the normalized radiance is its relative insensitivity to calibration error. It would be good to find a way of estimating the derivative $\frac{\partial N}{\partial \nu}$ in Eq. (5.3) without precise knowledge of the brightness temperature. From the discussion in the previous paragraph it would seem possible to substitute the information about attenuation length, temperature gradient, and base state temperature in place of brightness temperature.

To achieve this end $N(\nu)$ curves were computed as discussed earlier for several different attenuation lengths from $\chi = 1700m$ to $\chi = 8820m$. A regression line of form $b + m\nu$ was fit to each of these. It was found that the slope, m, of each of the regression lines increased linearly with increasing χ, as shown in Fig. 5.3. From this it is possible to find $m(\chi) = c\chi$, which gives

$$N(\nu) = b + c(\nabla T, T_o)\chi\nu \ . \tag{5.4}$$

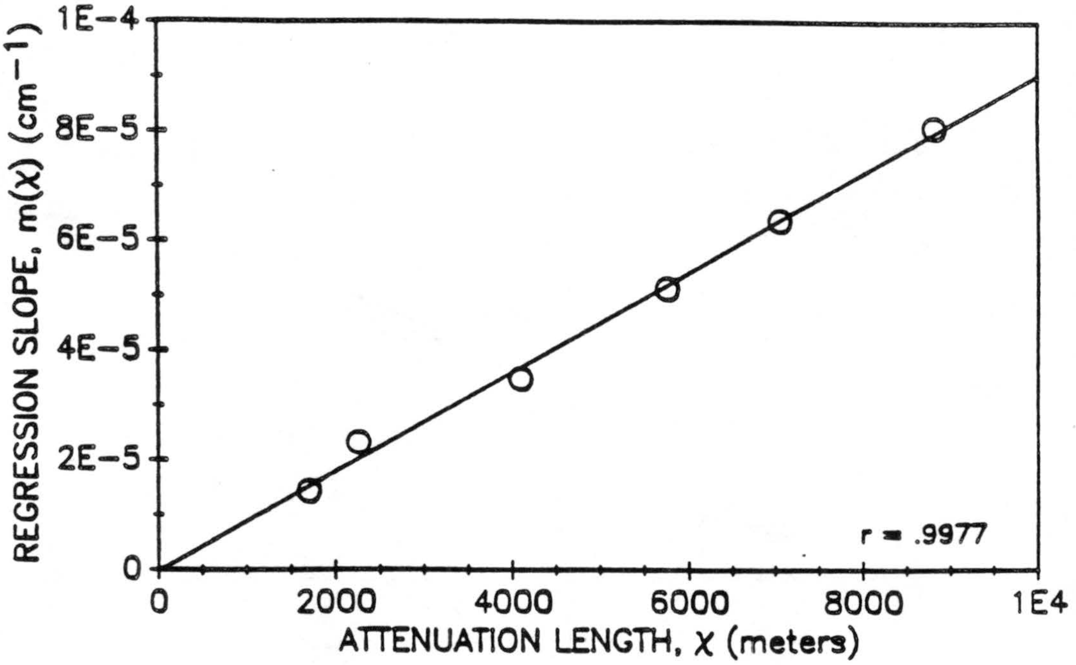

Figure 5.3: *Regression slope for correction to normalized radiance vs. attenuation length.*

Equation (5.4) is valid for only one temperature gradient and base state temperature. An equation of the form of Eq. (5.4) was generated for 4 different temperature gradients varying from .5 to 2 degrees per km. From these $c(\nabla T, T_o)$ was found to vary linearly with ∇T and was expressible in the form

$$c(\nabla T, T_o) = G(T_o)\nabla T + H(T_o) \ . \tag{5.5}$$

The remaining degree of freedom is that of the base state temperature T_o which determines the form of G(T_o) and H(T_o) in Eq. (5.5). To find G and H it was necessary to repeat the procedure described above for several temperatures ranging in 15°K increments from 250°K to 310°K. As shown in Figure 5.4 G(T_o) and H(T_o) are quite satisfactorily described by second order polynomials.

With the above work accomplished it is now possible to rewrite Eq. (5.4) as

$$N(\nu) = a + (G(T_o)\nabla T + H(T_o))\chi\nu \ . \tag{5.6}$$

Comparing Eq. (5.6) to Eq. (5.1) it is apparent that the quantity $(G(T_o)\nabla T + H(T_o))\chi$ is the approximation to $\frac{\partial N}{\partial \nu}$ which was being sought. Hence Eq. (5.1) can be recast as

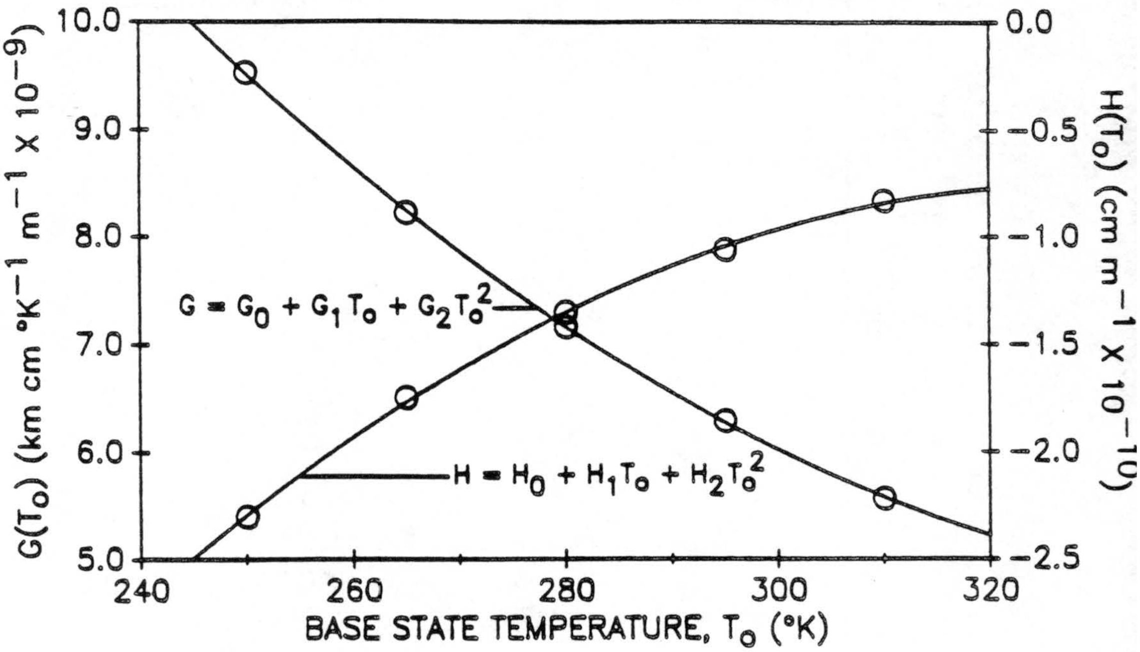

Figure 5.4: *Coefficients $H(T)$ and $G(T)$ vs. base state temperature.*

$$N(\nu) = N(\nu_o, T_o, T_B) + (\sum_{n=0}^{2} G_n T_o^n \nabla T + H_n T_o^n)\chi(\nu - \nu_o) . \tag{5.7}$$

The relative accuracy of this statistically estimated $\frac{\partial N}{\partial \nu}$ is shown as the short dashed line in Fig. 5.2. While not as accurate as Eq. (5.1) the approximation is still quite useful and does not require precise knowledge of T_B. The parameters used to find this statistical form are listed in Table 5.1 and the values of the G_n and H_n are listed in Table 5.2.

Rearranging Eq. (5.7) gives an alternate formula for the centered normalized radiance

$$N_c(T_o, T_B) = N(\nu, T_o, T_B) + (\sum_{n=0}^{2} G_n T_o^n \nabla T + H_n T_o^n)\chi(\nu - 650cm^{-1}) . \tag{5.8}$$

While the necessity of a priori knowledge of ∇T may seem to limit the usefulness of this form for determining temperature gradients the next chapter will demonstrate the utility of this approximation.

Table 5.1: Parameters used to derive the G_n and H_n coefficients.

ATTENUATION LENGTHS (METERS)	GRADIENT MAGNITUDES ($^\circ K/km$)	BASE STATE TEMPERATURES ($^\circ K$)
1700	.5	250
2260	1.0	265
4100	1.5	280
5760	2.0	295
7060		310
8820		

Table 5.2: G and H coefficients with T_o in degrees K, ∇T in degrees K/km, χ in meters and ν in inverse cm.

n	$G_n(T_o)$	$H_n(T_o)$
0	5.9182×10^{-8}	-2.7029×10^{-9}
1	-3.0591×10^{-10}	1.5931×10^{-11}
2	4.2897×10^{-13}	-2.4143×10^{-14}

Chapter 6

A STATISTICAL APPROACH TO INFERRING GRADIENT MAGNITUDE

Now that the radiative effects of horizontal temperature gradients have been demonstrated and the centered normalized radiance defined it is desirable to seek a mathematical relationship for radiance as a function of gradient magnitude. An examination of the radiance/azimuth angle curves shows a sinusoidal dependence of N(ϕ) on ϕ.

Figure 6.1 is a scatter plot of N(ϕ). Superimposed over this scatter plot is a cosine curve with an offset of one and an amplitude [(N(0°) - N(180°)] / 2 . As seen in this figure the cosine curve very closely fits the N(ϕ) data points. (The previously discussed curves have used cubic spline interpolation). Experimental evidence indicates that even for N(ϕ) amplitudes of .2, corresponding at this wave number to a gradient of about 15° C/km., over 90% of the weight in a cosine power series is given to the linear term.

The effective temperature gradient seen by an observer looking at an angle ϕ in the direction $\hat{r}$ is given by

$$\nabla T_{eff} = \hat{r} \cdot \vec{\nabla} T = \nabla T cos\phi . \tag{6.1}$$

From this and the cosine behavior seen in Fig. (6.1) one would expect a relationship of the form

$$N(\phi) = a \ \nabla T_{eff} + b . \tag{6.2}$$

to quite adequately describe the radiance dependency.

One possible technique for finding the coefficients a and b in (6.2) would be to expres all the terms in the radiative transfer equation in power series expansions and attempt t

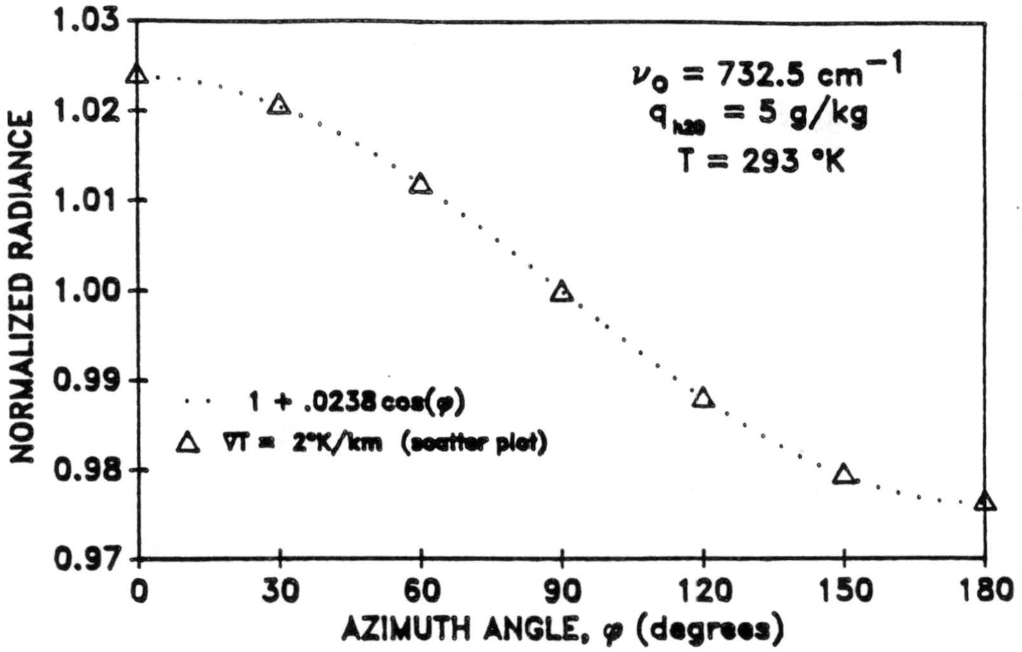

Figure 6.1: *Scatter plot of normalized radiance vs. azimuth angle and cosine fit to scatter data.*

integrate the equation analytically, discarding higher order terms involving the temperature gradient. Though this procedure is algebraically tedious it does yield an integral which can be evaluated exactly. Unfortunately the method also requires assumptions and simplifications that yield a result of limited diagnostic value. A brief summary of this method is given in Appendix A. The final result is

$$N_c(\phi) = 1 + \frac{C_2 \nu \chi}{T_o^2} \frac{|\nabla T|}{2} cos\phi \ . \tag{6.3}$$

This is indeed of the form of (6.1). Perhaps the most notable consequence of (6.15) is that the result shows no temperature dependency by density perturbations, pressure broadening or line intensity. (All of this dependency is "traced" by the coefficient η defined in Appendix A. Note that η does not appear in (6.15)).

In practice this approach has not proved very useful. It is difficult to find a correct value for the mass absorption coefficient when more than one emitting gas is present. Also, as indicated by Smith (1969) and discussed in Chap. 4 the linear relationship of optical thickness on geometric length assumed when defining the mass absorption coefficient, k_ν, is a simplification which is not borne out in modelling results.

For the example frequently used before with $q_{H_2O} = 5g/kg$, $\chi = 2420\ m$, $\nu_o = 732.5\ cm^{-1}$ and $\nabla T = 1°C/km$ equation (6.3) gives $N_c(0°) = 1.019$ compared to a model output result of 1.012. Inverting (6.3) for ∇T and using $N_c(0°) = 1.012$ (the modelling result, presumably correct) gives a value of .63° C/km for ∇T. This is about 40% too small. The results of this method also tend to deteriorate as χ becomes large. Also a pressure dependency in radiative transfer calculations is expected, yet there is no such pressure term in Eq. (6.3). For these reasons another method must be found to derive a relationship of the form (6.2).

Since the attenuation length χ is not in general a measurable quantity in the field and must be calculated it is a less desirable parameter than one which can be directly measured. Nonetheless χ was shown to be an important parameter for characterizing the spectral emittance as its presence in Eq. (6.3) indicates. Figures 6.2 and 6.3 show $N_c(0°)$ plotted as a function of χ for $\nabla T = 1°$ K/km and the two base state atmospheres frequently used as examples before. A least squares line is also fitted to each scatter plot. A nearly linear relationship between attenuation length and centered normalized radiance is exhibited with a correlation value exceeding .99 for both plots. Further the least squares line

$$N_c = A\chi + B \tag{6.4}$$

in both plots has almost the same slope A. That these two cases differ significantly in the humidity of their respective atmospheres and yet the functional relationship is almost identical implies an invariance of this relationship to absolute humidity changes. (Recall that χ is a function of q_{H_2O} and implicitly contains information about humidity.)

From the results of the preceeding discussion one would expect the slope of the regression lines A to be proportional to the magnitude of the temperature gradient, that is $A = f^{cn}(\nabla T)$ and indeed this is the case. Figure 6.4 shows a plot of A(∇T) for several values of ∇T, all other parameters remaining constant. Again a very linear relationship occurs:

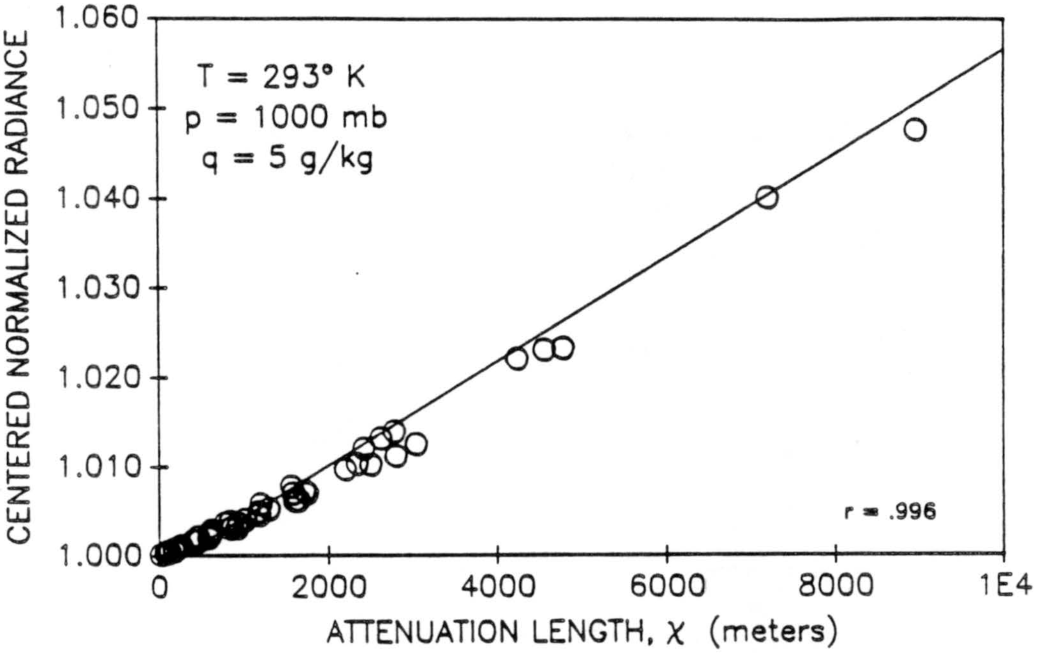

Figure 6.2: *Centered normalized radiance vs. attenuation length for a water vapor mixing ratio of 5 g/kg.*

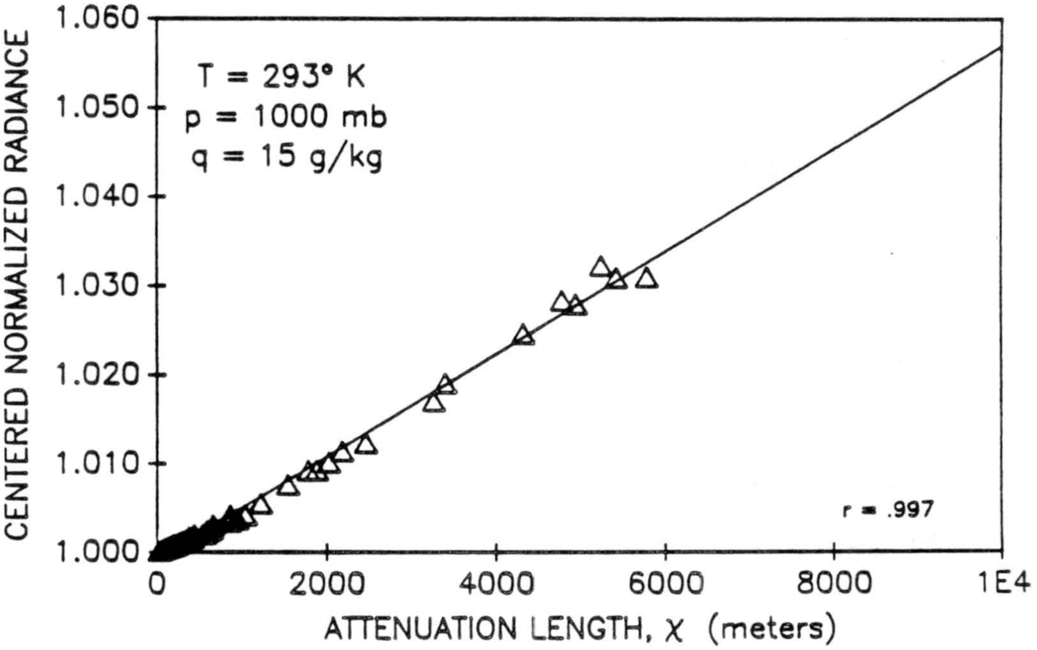

Figure 6.3: *Centered normalized radiance vs. attenuation length for a water vapor mixing ratio of 15 g/kg.*

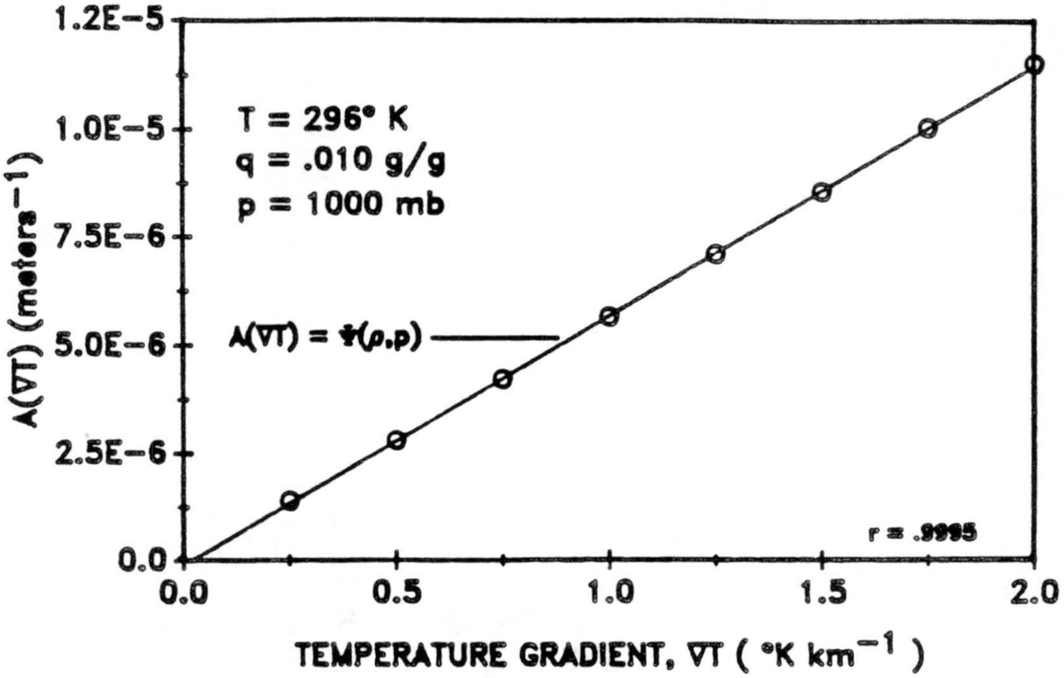

Figure 6.4: *Regression slope A vs. temperature gradient magnitude.*

$$A(\nabla T) = \Psi \cdot \nabla T + C, \qquad C \approx 0\,. \tag{6.5}$$

Up until this point the base state temperature T_o and pressure p have been considered constant. The base state density $\rho_o = \frac{p}{R_d T_v}$ has varied somewhat through the dependence of virtual temperature T_v on the mixing ratio via the relationship

$$T_v = T_o(1 + .61 q_{H_2O})\,. \tag{6.6}$$

The next step is to quantify the behavior of the proportionality constant Ψ as pressure is held fixed and density is varied through changes in T_v and q_{H_2O}. The least squares method is most sensitive to the data points furthest from the origin. Since the most pertinent attenuation lengths for this work are between 800 and 5000 meters data were filtered so that only these points were used in calculating the slopes of the least squares lines. This does not impose any significant restrictions on the use of attenuation lengths outside this range but merely eliminates the noise associated with the bias towards these large χ. Indeed with the exception of the smallest H_2O mixing ratios almost all χs are less than 5000 m. The limit on the minimum magnitude of attenuation lengths eliminates those χ

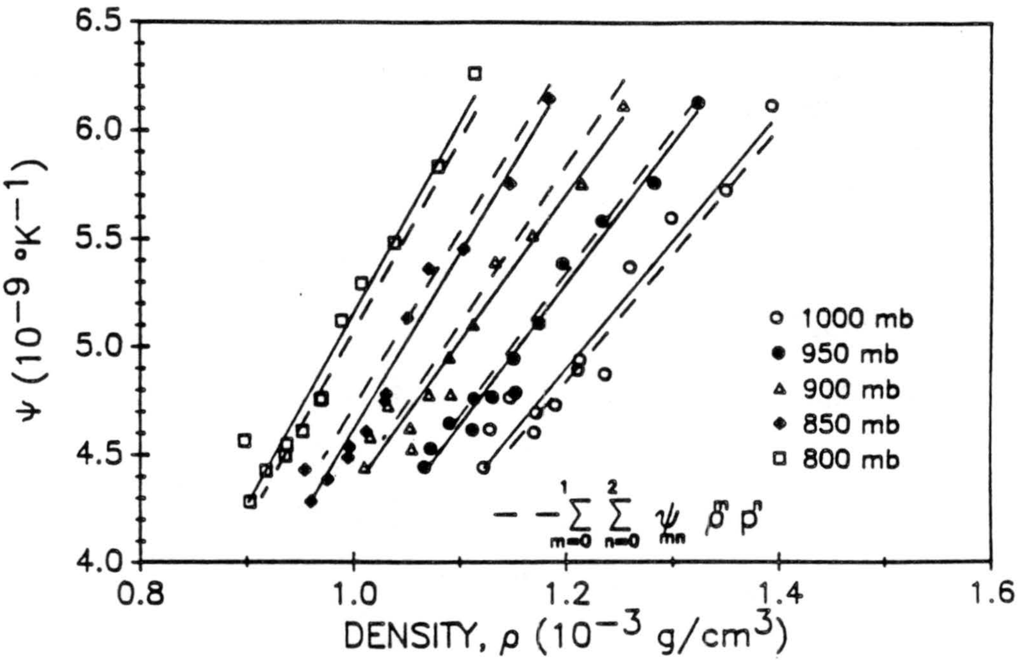

Figure 6.5: $\Psi(\rho)$ *for pressures from 800 mb. to 1000 mb.*

most sensitive to the quantization error. The need for extremely sensitive instrumentation also puts a practical constraint on the use of these diminutive attenuation lengths. Again many of these small χ are still well approximated by the fitted curve.

In Figure 6.5 plots of $\Psi(p,\rho)$ are shown for several fixed pressures as the associated densities are varied. Though somewhat noisy the data points are quite reasonably approximated by a first degree polynomial:

$$\Psi(p,\rho) = \psi_o + \psi_1\rho = \sum_{m=0}^{1} \psi_m \rho^m \, . \tag{6.7}$$

Here $\psi_m = f^{cn}(p)$,that is the ψ_m vary as pressure changes. The solid lines connecting the data points in Fig. 6.5 are linear regressions of the form of Eq. (6.7).

The last task remaining is to find a functional relationship for the ψ_m in terms of pressure. The even spacing of the $\Psi(p,\rho)$ plots in Fig. 6.5 suggests that there exists a fairly simple pressure relationship among the curves. Second order regressions for ψ_o, and ψ_1 give a good fit to the data. With this result it is possible to write

$$\psi_m = Z_o + Z_1 p + Z_2 p^2 = \sum_{n=0}^{2} Z_n p^n \, . \tag{6.8}$$

Table 6.1: The Ψ coefficients, $\psi_{m,n}$

$\psi_{m,n}$	n	0	1	2
m				
0		-1.002×10^{-5}	7.8032×10^{-9}	1.053×10^{-15}
1		2.0712×10^{-2}	-1.4833×10^{-5}	4.195×10^{-10}

Now, defining the 2×3 matrix $\psi_{mn} = \psi_m Z_n$, $\Psi(p, \rho)$ can be written as

$$\Psi(p, \rho) = \sum_{m=0}^{1} \sum_{n=0}^{2} \psi_{mn} \rho^m p^n. \tag{6.9}$$

The values of the $\psi_{m,n}$ are listed in Table 6.1.

To test the validity of (6.9) Ψ was calculated for the pressures listed in Fig. 6.5. These are the dashed curves which reveal a reasonable fit to the data points. Combining the preceding results allows Eq. (6.4) to be written in the form

$$N_c = \left(\sum_{m,n=0}^{2,2} \rho^m p^n \right) \chi(\nu, q_{H_2O}, T) \nabla T \cos\phi + (1 - .002 \cos\phi) \ . \tag{6.10}$$

The intercept B in Eq. (6.4) was found to give best results when

$$B(\phi) = 1 - .002 \cos\phi$$

It is interesting to contrast Eq. (6.10) with Eq. (6.3), the polynomial approximation result. The statistical approach replaces the prefactor $\frac{C_2 \nu}{2T_o^2}$ with the double sum of $\Psi(p, \rho)$. As mentioned earlier the pressure broadening effects and line intensity effects dropped out of the polynomial solution when nonlinear terms in the reduced temperature gradient Φ were truncated. Thus the resulting solution Eq. (6.3) did not have any pressure dependency. Ψ however is an explicit function of pressure and density giving Eq. (6.10) a pressure dependency not seen in (6.3). Eq. (6.3) also has a somewhat more complicated implicit temperature and density form.

Table 6.2: Parameters used in deriving the $\psi_{m,n}$

Base State Temperature $(^\circ K)$	Mixing Ratio (g/kg)	Gradient Magnitudes $(^\circ K/km)$	Pressures mb
250	.5	.25	800
258	.7	.50	850
268	2.0	.75	900
276	3.5	1.00	950
281	5.0	1.25	1000
286	7.5	1.50	
286	10.0	1.75	
291	10.0	2.00	
296	7.5		
301	15.0		
306	15.0		
306	25.0		

The useful domain for this statistical result is determined by the range in data points used in deriving (6.9). The parameters used in generating the data sets are listed in Table 6.2. Temperatures varied from 250° K to 311° K, water vapor mixing ratios varied from 0.2 g/kg to 35 g/kg and pressures varied from 800 mb to 1000 mb. The wave number range was 500 cm^{-1} to 800 cm^{-1}. This domain encompasses almost all conditions of interest found in the boundary layer.

Atmospheres with temperatures less than 0°C tend to have much larger attenuation lengths due to the paucity of humidity imposed by the Clausius–Clapeyron equation. This upper bound on humidity somewhat limits the choice of useful attenuation lengths since such large χ may extend well beyond the gradient being measured. (However the possibility of humidity variations is also greatly reduced.) Since saturation mixing ratios roughly double every 10°C the other end of the temperature range has relatively small attenuation lengths for mixing ratios common in tropical settings. In these situations the choice of attenuation lengths suitable for measuring small magnitude temperature gradients of large extent is also more limited. In most conceivable mid-latitude settings the range of attenuation lengths is adequate for most all boundary layer phenomena.

Note that Eq. (6.10) is in terms of the centered normalized radiance $N_c(\phi)$ while the field–measurable variable is the normalized radiance $N(\phi)$. Combining Eq. (6.10) and Eq. (5.8) gives

$$N(\nu,T_o,T_B) + (\sum_{n=0}^{2} G_n T_o^n \nabla T + H_n T_o^n)\chi(\nu - 650cm^{-1})$$

$$= \left(\sum_{m,n=0}^{2,2} \rho^m p^n \right) \chi(\nu, q_{H_2O}, T)\nabla T \cos\phi + (1 - .002\cos\phi) \ . \qquad (6.11)$$

Solving Eq. (6.11) for the temperature gradient magnitude gives the result

$$\nabla T = \frac{N(\phi) - \sum_{n=0}^{2} H_n T_o^n - (1 - .002\cos\phi)}{[(\nu - 650cm^{-1})\sum_{n=0}^{2} G_n T_o^n + \sum_{m,n=0}^{1,2} \psi_{m,n}\rho^m p^n]\chi\cos\phi} \ . \qquad (6.12)$$

The utility of Eq. (6.12) for field measurements is evident. The attenuation length $\chi(\rho, T, q_{H_2O})$, $\Psi(\rho, p)$, $G(T_o)$ and $H(T_o)$ can be calculated in a few seconds with the aid of a micro-computer (or tabulated results used) once the local field variable are known. Two radiance measurements are required to determine N(ϕ). For best results N(ϕ) should be maximized by choosing a value for ϕ of 0° or 180°. This necessitates measuring directly up or down the gradient. A rapid azimuthal scan gives a good approximation to the geometric orientation of the temperature gradient and hence ϕ. Over relatively smooth terrain or water, ground observations will yield a good approximation through the thermal wind equation. Frequently this orientation is known a priori. If values of the local field variables are relatively static, χ, ψ, $G(T_o)$ and $H(T_o)$ and R(90°) remain constant and ∇T(t) can be measured in real time with a minimum of signal processing.

Combining Eq. (6.10) and Eq. (5.3) and solving for ∇T yields

$$\nabla T = \frac{N(\phi) - \left[\frac{\partial N}{\partial \nu}\right]_{\nu_o = 650cm^{-1}, T_o, T_B} (\nu - 650cm^{-1}) - (1 - .002\cos\phi)}{\sum_{m,n=0}^{1,2} \psi_{m,n}\rho^m p^n \ \chi \ \cos\phi} \ . \qquad (6.13$$

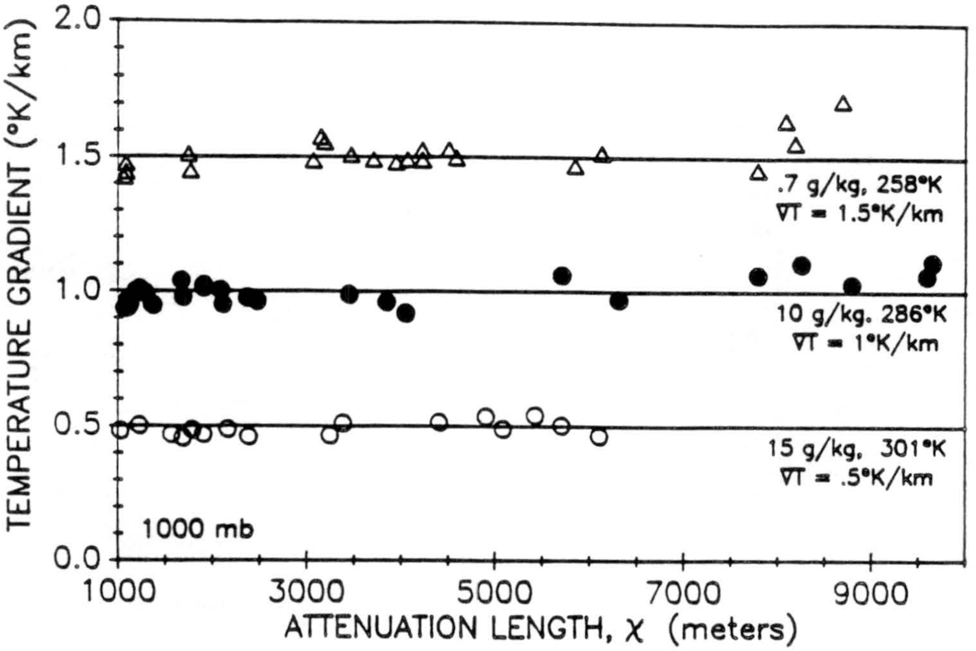

Figure 6.6: *Inferred temperature gradient vs. attenuation length for a pressure of 1000 mb.*

If the measuring instrument is precisely calibrated and an accurate estimate of the brightness temperature T_B is possible, Eq.(6.13) offers an alternate method of inferring ∇T.

To test the accuracy of Eq. (6.12) normalized radiances were calculated for a variety of atmospheric conditions, attenuation lengths, and gradient magnitudes. Figure 6.6 – Figure 6.10 show a summary of these results. For each of five different pressures from 800 to 1000 mb three different base states with differing imposed temperature gradients were examined. The solid lines in each panel indicate the correct value of ∇T which Eq. (6.12) is attempting to reproduce. The method is quite accurate for attenuation lengths in excess of about 1200 meters. In terms of percent accuracy almost all inferred gradients were within 10% of the actual value. As expected the absolute error is greatest for the largest gradients.

Though attenuation lengths of $\chi \geq 5000\ m$ were filtered out in the statistical procedure, Figs. 6.6 – 6.10 indicate that these attenuation lengths are still quite useful for gradient inference. The role of pressure in the distribution of attenuation lengths is demonstrated by the $q_{H_2O} = 15\ g/kg$ plots. For 1000 mb of pressure there are no attenuation

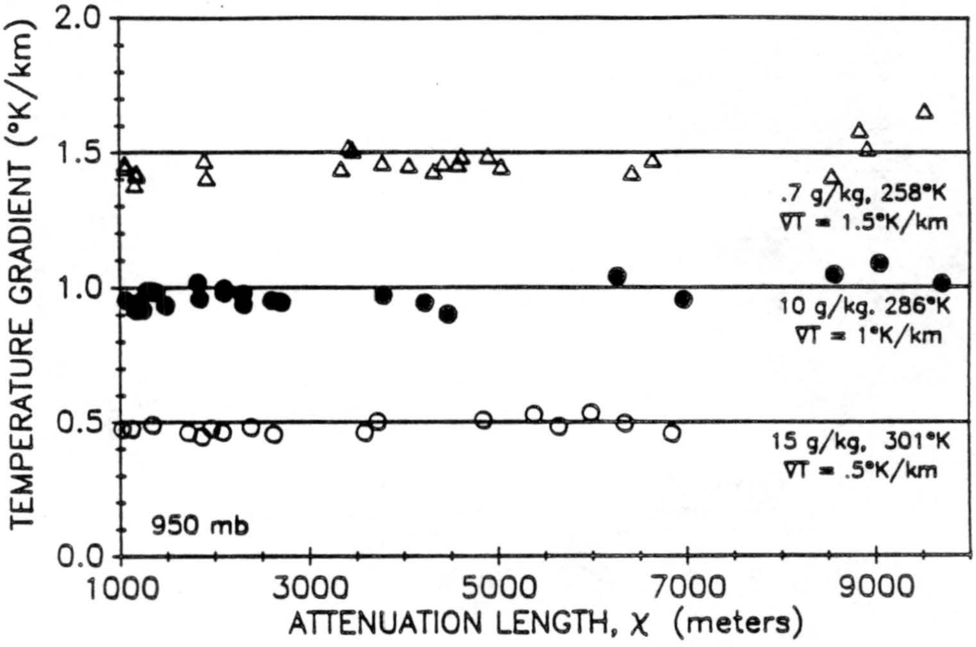

Figure 6.7: *Inferred temperature gradient vs. attenuation length for a pressure of 950 mb.*

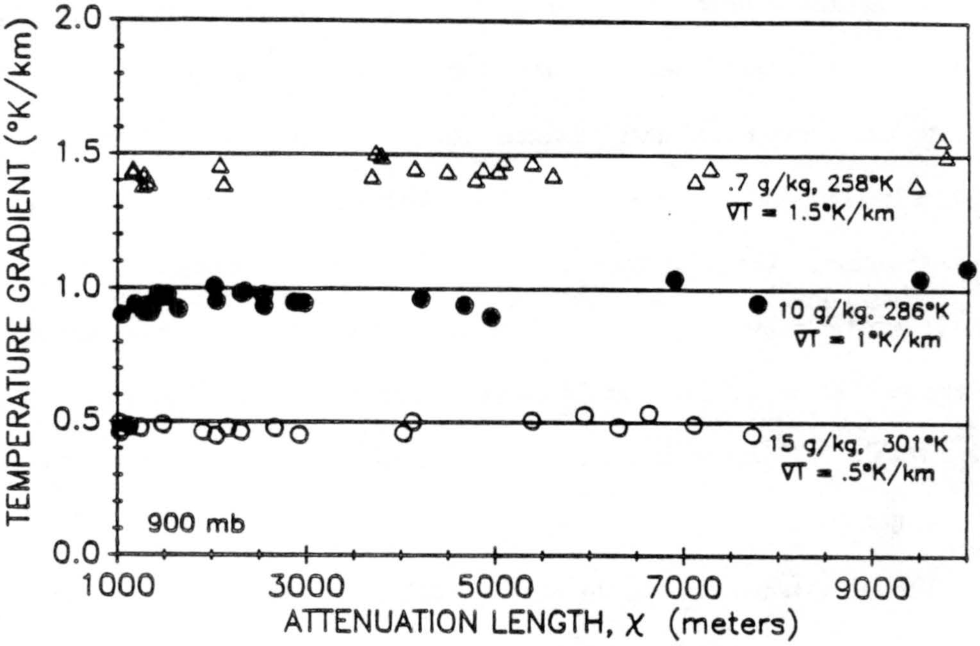

Figure 6.8: *Inferred temperature gradient vs. attenuation length for a pressure of 900 mb.*

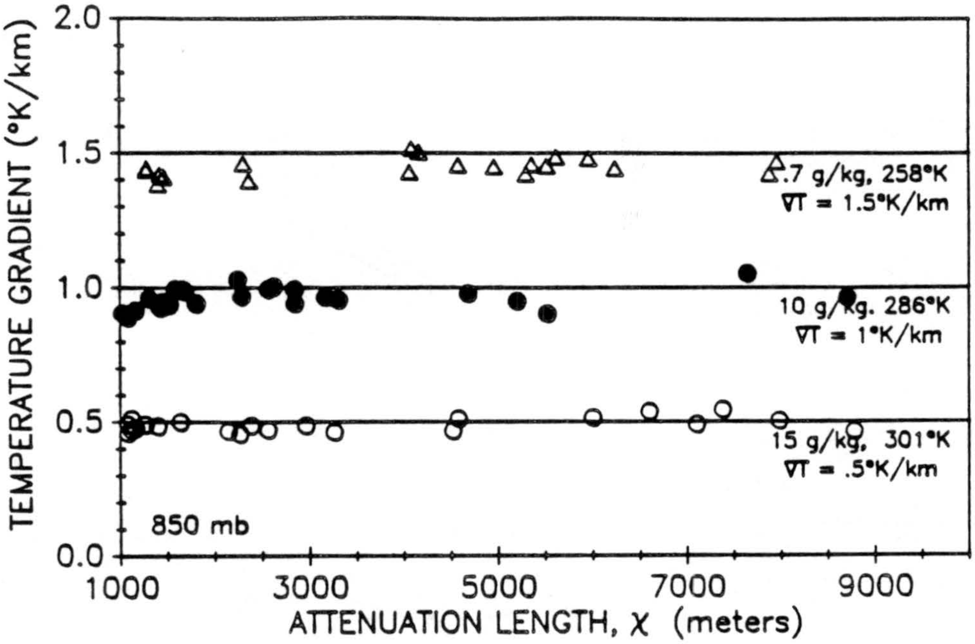

Figure 6.9: *Inferred temperature gradient vs. attenuation length for a pressure of 850 mb.*

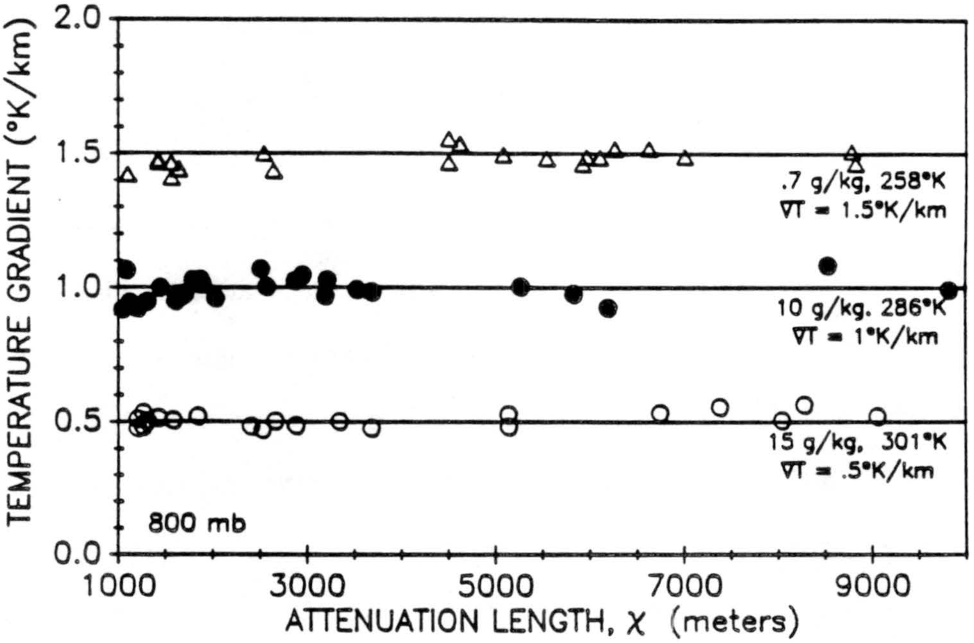

Figure 6.10: *Inferred temperature gradient vs. attenuation length for a pressure of 800 mb.*

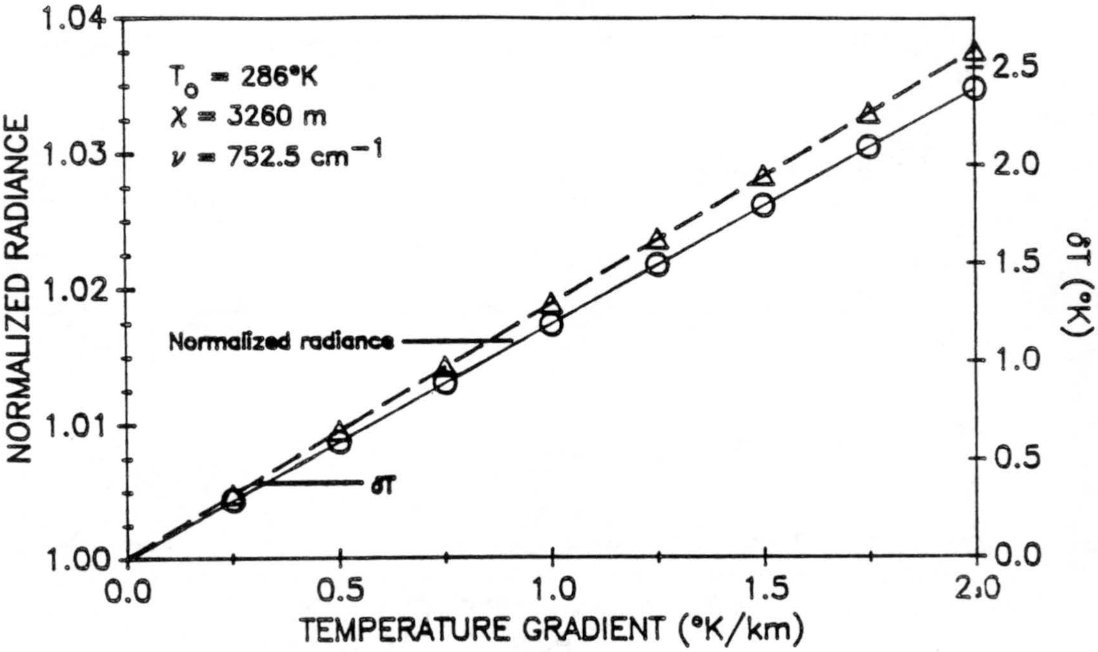

Figure 6.11: ***Normalized radiance and δT as a function of temperature gradient magnitude.***

lengths greater than about 6000 meters where the 800 mb case shows several χ which exceed this value. As mixing ratios decline, as in the $q_{H_2O} = .7\ g/kg$ cases, the pressure dependency of the χ distribution is not nearly as pronounced.

In all cases the results deteriorated as χ became small. At the extreme short end of the χ range (those values not plotted in Figs. 6.6 – 6.10) some errors were in excess of 500% probably due to discretization errors in the attenuation length calculations as the result of finite model resolution. From a practical standpoint this is not important since for such small χ, gradients would need to be of exceedingly large magnitude to yield normalized radiances significantly greater than unity. Figs. 6.6 – 6.10 indicate that in nearly all cases there are a variety of attenuation lengths $\chi(\nu)$ from which to choose as the individual situation warrants.

Figure 6.11 shows the normalized radiance and δT (as defined by Eq. 4.6) plotted as a function of gradient magnitude for an attenuation length of 3260 meters. From this figure it is possible to determine the instrument sensitivity required to detect and measure temperature gradients. For a gradient magnitude of $.5° K/km$ the normalized radiance is

about 1.0075 and δT about $.5^\circ K$. To even detect this gradient the radiometer must be able to detect a .75% difference in radiance values or equivalently a $.5^\circ K$ difference in radiative temperatures. For a gradient of $2^\circ K/km$, $N(0^\circ)$ is about 1.035 and δT about $2.5^\circ K$ implying a threshold sensitivity of about 3.5%. For a measurement accuracy of ±10% the sensitivity must be 10–fold greater than the threshold N and δT values.

Chapter 7

SOURCES OF ERROR IN THE DETECTION OF TEMPERATURE GRADIENTS

In the last chapter an equation was derived which related the magnitude of a temperature gradient to various measured and calculated quantities. The purpose of this section is to consider the effects of error and noise in the measurement process and how these impact on the results of Eq. (6.12).

It is reasonable to assume that the basic field variables T, p, and q_{H_2O} can be measured to within the required tolerances using readily available instrumentation. The effect of dust, aerosols, and small cloud droplets is much more difficult to quantitively measure and will generally act to reduce the attenuation length. If compensation is made for this scattering, the accuracy to within which the attenuation length χ can be calculated is likely limited by the scheme which finds transmittances. For a gradient of measurable magnitude the direction of the gradient should be evident and hence the angle ϕ fairly well defined.

By far the greatest uncertainty arises in the measurement of $R(0°)$ and $R(90°)$ which are needed to compute $N(\phi)$. The greatest "contrast" or most extreme value of $N(\phi)$ occurs for $\phi = 0°$ or 180°, that is a measurement parallel or antiparallel to the gradient. The inference of ∇T using Eq. (6.12) requires finding a small difference between two large numbers. As a result the accuracy of the equation is enhanced when N has its extreme value making this difference the greatest. Therefore it is preferable to use $N(0°)$ or $N(180°)$ in Eq. (6.12).

Several techniques and methods such as signal processing and averaging have been developed to decrease or minimize the uncertainty in results introduced by the measuring instrumentation (ex. Arams, 1973). Such techniques also help to reduce uncertainty due to the random variability of the phenomena being measured. A detailed discussion of these techniques requires the specification of particular hardware and electronics characteristics. In the interest of keeping the discussion general the term noise will here refer to any signal artifact which remains after such processing has occurred.

The magnitude of $N(\phi)$ is a function of both $\chi(\nu)$ and ∇T. As $\nabla T \rightarrow 0$, $R(0°) \rightarrow R(180°)$ and $N(\phi) \rightarrow 1$. The minimum detectable gradient for a given χ is usually determined by the dark noise signal of the radiometer. (Dark noise is the residual output signal of the instrumentation with no input radiance). Defining $\mathcal{Q}$ as the radiometer output due to a radiance input of S and $\delta R = R(0°) - R(90°)$ the signal output of the radiometer for $R(0°)$ is

$$\mathcal{Q}(R(0°)) = \mathcal{Q}(R(90°) + \delta R(\nabla T)) = \mathcal{Q}(R(90°)) + \delta \mathcal{Q}(\nabla T) . \tag{7.1}$$

Now if the random noise introduced into the output signal by the detection and amplification is given by δN then the output of the radiometer due to both the input signal S and noise artifact is $\mathcal{Q}(S) + \delta N$. When $\delta \mathcal{Q}(\delta T)$ in (7.1) is of the same size as δN the difference $\mathcal{Q}(0°) - \mathcal{Q}(90°)$ is not detectable apart from the noise. This means that for a given δN there exists a threshold temperature gradient below which ∇T is not measurable. As mentioned in Chapter 3, as the measured bandwidth $\delta \nu$ is increased the input power δS is increased. Since the dark noise caused by the detection and amplification circuitry is independent of the input power, increasing the bandwidth increases $\delta \mathcal{Q}$ while keeping δN constant.

The temperature sensitivity, S_t, another figure of merit sometimes specified for radiometers, is the minimum resolvable temperature difference. For the application being discussed in this work the largest acceptable temperature sensitivity for gradient detection would be the difference between the brightness temperature $T_B(\phi)$ and the base state temperature T_o. For confidence in the magnitude measurement the temperature sensitivity would of course need to be considerably smaller. S_t is sometimes misleading as temperature sensitivity is a itself a function of temperature and only has comparative value when the temperature is also specified. Also the radiance from a target at $1000^\circ K$ is an order of magnitude larger than a terrestrial target putting the signal much higher above the noise floor. Many radiometers developed for use in industrial settings lack the necessary temperature sensitivity at terrestrial temperatures. This instrumentation limit is probably the determining factor in the ability of passive radiometric techniques to infer horizontal temperature gradients. As more sensitive field deployable instruments are developed the threshold gradient magnitude will become much lower giving this method a wider base of applications.

Another source of error in estimating gradients is the random time variability of the atmospheric temperature along the line of sight of the radiance measurement. In a stable atmosphere, for example in the nocturnal boundary layer, very little short term temperature variation would be expected. In contrast, the solar forced boundary layer on a hot summer afternoon is characterized by a superadiabatic lapse rate. This gives rise to a constant convective adjustment or overturning in the boundary layer. Such motions permit short term variations of up to 1 degree C in the local temperature. The length scale of these dry convective cells varies with wind conditions, zenith angle of the sun and surface inhomogeneities.

The effects of such a variation on the radiance depend on $\chi(\nu)$. For a large attenuation length the effect should be minimal since the sum of many such random perturbations approaches zero. As the attenuation decreases the radiance becomes much more sensitive to such perturbations, especially close to the point of detection. Figures 7.1 and 7.2 show the effects of such random temperature variations. Both figures show 25 different scan simulations. A random temperature noise with maximum possible amplitude of 1° C was

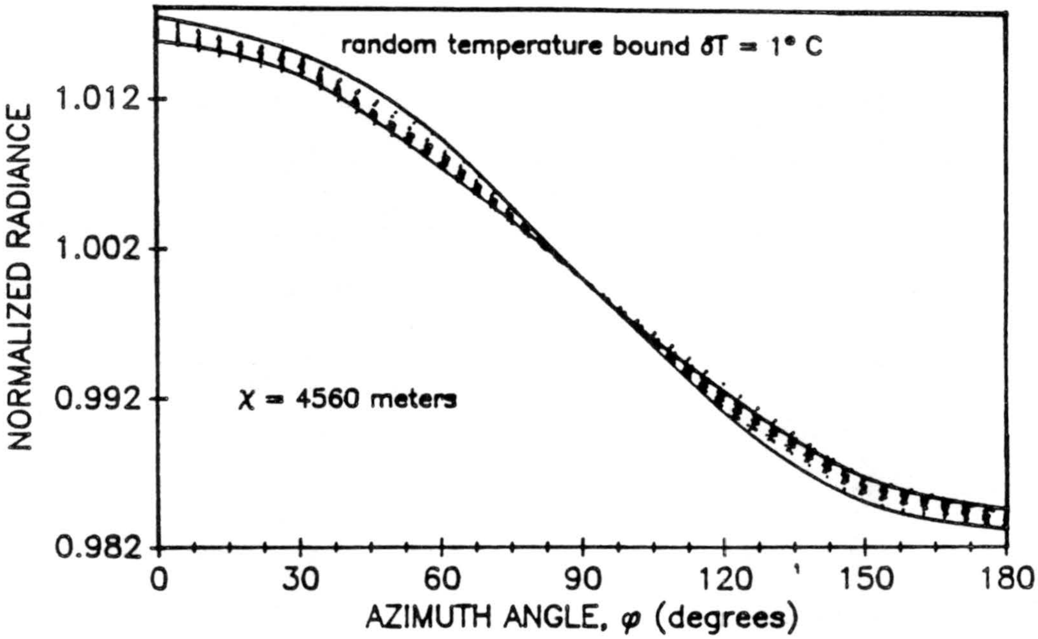

Figure 7.1: *Several plots of normalized radiance with random temperature noise vs. azimuth angle for an attenuation length of $\chi = 4560$ m.*

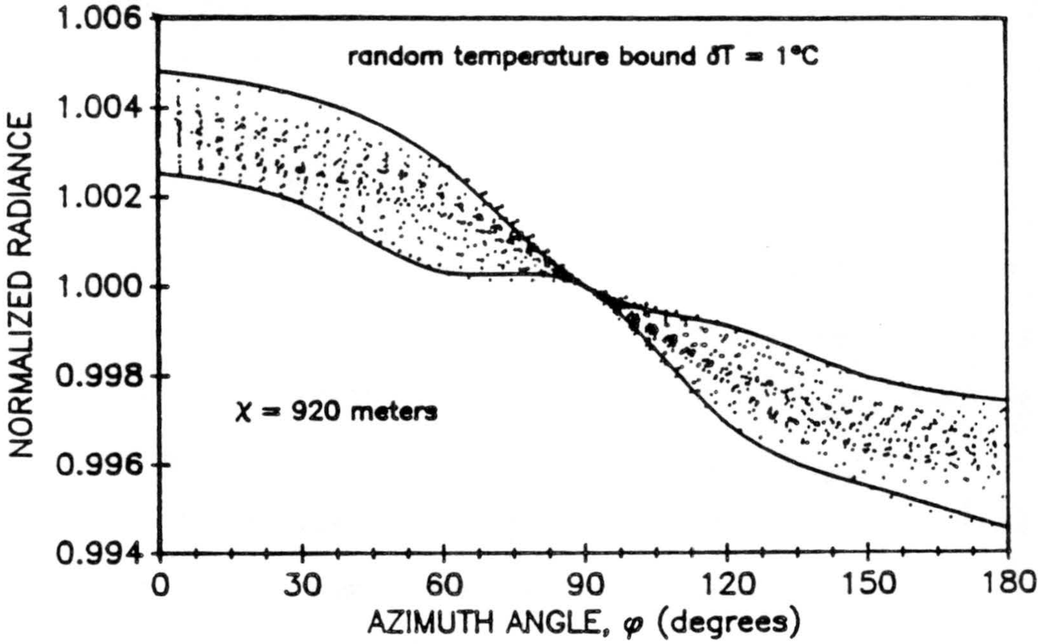

Figure 7.2: *Several plots of normalized radiance with random temperature noise vs. azimuth angle for an attenuation length $\chi = 920$ m.*

imposed on the base state temperature field and temperature gradient. Figure 7.1 is the case of a long attenuation length with $\chi = 4560$ meters. Figure 7.2 is the case of a short attenuation length; $\chi = 920$ meters. It is evident that the random perturbation gives a much greater uncertainty in the case of a short attenuation length.

It should be noted that the lifetime of these perturbations can be from several seconds for a small length scale to perhaps a few minutes for a very large scale length. The distinction between large scale long lived temperature perturbations and the underlying horizontal temperature gradient is not clear and must ultimately be determined by the time and length scale of the gradient of interest. Also to consider this temperature variability as noise the perturbation coherence length or distance over which there exists a positive correlation for these temperature transients should be much smaller than the attenuation length. For small scale and rapidly varying perturbations of a random nature which can truly be considered noise, the averaging of several scans should produce a result closely approximating the noise-free scan. This method may indeed prove to be a useful tool in studying the short term temporal and spatial variability in the convectively active boundary layer.

The final atmospheric noise problem to contend with is that of water vapor mixing ratio variability. Local random variations in humidity occur in much the same fashion and for many of the same reasons as the temperature variations just discussed. In areas where the surface is wet much of the incoming solar radiation is used to evaporate water rather than to heat the surface. While this somewhat reduces convective activity the resulting convective cells can show a large increase in moisture over their surroundings. Modeling experiments show little sensitivity to these random variations.

A more serious problem is that of a water vapor gradient of the same length scale as the temperature gradient being measured. As previously mentioned there are several instances where temperature and water vapor gradients coincide such as in thunderstorm downbursts and along frontal boundaries. The problem induced as a result of such a water vapor gradient is that the attenuation length now becomes a function of the azimuthal angle ϕ. The reduced temperature gradient $\Phi = \frac{\nabla T}{T_o}$ defined in Eq. (A.3) has a typical value on the order of 10^{-3}. The analogous reduced H_2O mixing ratio gradient $\frac{\nabla q}{q_o}$ is on the order of 10^{-1} which makes this perturbation quite significant. Even when q_{H_2O} is constant a slight azimuthal variation in χ occurs due to the temperature induced density variation. In those bands which show a sensitivity to H_2O concentrations this variation is several orders of magnitude less than that caused by even a modest water vapor gradient imposed on a relatively dry basic state atmosphere. The effect of such an azimuthal χ dependency is to a large extent a function of the relative orientation of $\vec{\nabla} T$ with respect to $\vec{\nabla} q_{H_2O}$. A mixing ratio gradient is usually evidenced by an asymmetry in the scan curve either as a difference in the oscillation amplitude between $N(0°)$ and $N(180°)$ or as a difference between the curves $N(0°) \longrightarrow N(180°)$ and $N(180°) \longrightarrow N(360°)$. A nonconstant $\vec{\nabla} T$ can also produce similar results independent of a mixing ratio gradient and the two effects are difficult to deconvolve from radiometric measurements alone. Utilization of a band which has minimal water vapor dependence will decrease these effects.

In addition to the error inducing factors described above any violation of the initial assumptions described in Chapter 3 will also induce error. Even a small error in leveling the radiometer can result in contaminated radiance measurements. When this occurs the scan plane is not horizontal, allowing the large vertical temperature variation in temperature to overshadow the smaller azimuthal temperature variation. In an atmosphere with a heavy aerosol burden the calculation of χ which assumes no scattering will give a result which is larger than the true attenuation length. Using this χ in Eq. (6.12) the gradient will be underestimated. Violating the assumption of a unidirectional ∇T can cause significant errors. For example a scan of a temperature gradient with azimuthal symmetry from the center will show no variation of N(ϕ) regardless of the gradient magnitude. Other as yet undiscovered error sources will likely come to light as the technique is used in the field.

Chapter 8

SUMMARY AND DISCUSSION OF FUTURE WORK

The purpose of this work has been to investigate the impact of horizontal temperature gradients on the infrared radiance properties of the boundary layer and devise a scheme for inferring the gradient magnitude from these radiance properties.

The temperature and spectral dependence of the radiance of various atmospheric constituents was examined. The IR portion of the spectrum $500cm^{-1} \leq \nu \leq 800cm^{-1}$ was shown to be most sensitive to temperature induced radiance changes. This portion of the spectrum is also where the spectral energy density is greatest for terrestrial temperatures. The two important radiating gases at these wavenumbers are CO_2 and H_2O, the former having an almost constant mixing ratio while the latter has a highly variable mixing ratio in the boundary layer.

A model was described which numerically calculates the spectral radiances of CO_2 and H_2O in the atmosphere from $500cm^{-1} \leq \nu \leq 800cm^{-1}$. Using this model radiances on a constant pressure surface were calculated as a function of azimuth angle for a horizontally homogeneous atmosphere with an imposed temperature gradient. The normalized radiance $N(\phi)$, the radiance at azimuth angle ϕ divided by the radiance orthogonal to the gradient, was defined. The attenuation or e^{-2} folding length χ was introduced as a convenient parameter to characterize the spectral transmittance for a given set of physical conditions. Model calculations demonstrated that the normalized radiance has a linear dependence on the effective temperature gradient.

For a given attenuation length it was shown that the normalized radiance is a function of wavenumber. Two methods were derived to refer $N(\phi)$ to the normalized radiance $N_c(\phi)$

at $\nu = 650 cm^{-1}$, the center of the spectral region of interest. The first of these methods involved the use of the brightness temperature T_B as an observable quantity. The second method, derived using statistical techniques, did not require the knowlege of T_B.

Using the centered normalized radiance and the attenuation length, a scheme was devised which permitted the inference of temperature gradient magnitude from azimuthal radiance measurements and local values of humidity, pressure and temperature. The success of this technique was demonstrated by the accurate recovery of gradient magnitudes from calculated radiance data. It was shown that for an attenuation length of 3260 m a radiometric sensitivity of .75% or $.5^\circ K$ is required to detect a gradient of magnitude $.5^\circ K/km$. For a gradient magnitude of $2^\circ K/km$ a threshold sensitivity of 3.5% or about $2.5^\circ K$ is required. To quantitively measure the gradient to within 10% the sensitivity must be about .075% and .35% respectively for these two cases.

A field test of this method is the next logical step towards the realization of the real time measurement of horizontal gradients. This would require an independent second method of establishing the surrounding temperature field as well as a location where such gradients frequently occur. As alluded to in the previous chapter the sensitivity of a suitable radiometer is a major constraint on the feasibility of this application. Though such instruments do exist, they frequently tend to require a laboratory environment for operation. For working in the field an instrument is required which is easily portable and has modest power requirements and can operate in a wide variety of sometimes adverse ambient conditions.

Though the sensitivity of current microwave radiometers is not quite adequate for this application, rapid advances in satellite borne microwave radiometer technology should soon enable microwave devices to attain the necessary sensitivity for this purpose. Use of the longer wavelengths in the microwave spectrum would have several advantages. The Rayleigh–Jeans law, long wavelength (small wavenumber) approximation to the Planck function is much easier to use in analytical calculations, possibly permitting easier inversion of the radiative transfer integral. The error induced by scattering should be less for centimeter wavelengths. Finally the error induced by the variable nature of water vapor distribution could be eliminated by using a pass band which has no H_2O radiance contribution. For example the wings of the O_2 absorption bands at 60 or 118 Ghz would be appropriate since oxygen, like CO_2, is usually found in locally uniform mixing ratios in the boundary layer.

The bandwidth resolution used in this work is 5 cm^{-1} which is the resolution of the spectral transmittance scheme. Some radiometric devices such as interferometers have a spectral resolution less than 1 cm^{-1}. Using such a device might allow the user to select narrow bandpasses in the 500 cm^{-1} to 800 cm^{-1} spectral region where water vapor emittance is negligible and yet attenuation lengths are suitable for temperature gradient determination.

The normalized radiance, defined in this work as the ratio of $R(\phi)$ to $R(90°)$, is only one method of using measured radiances in determining horizontal temperature gradients. Though not explored here other normalizations or ratios might also be useful. For example the ratio of radiances measured at identical azimuth angles but differing center wavenumbers and attenuation lengths could, in principle, be used. This would not require scanning through a range of azimuth angles and would allow the measurement process to be less sensitive to radiometer leveling error. Such a technique would however require a thorough knowledge of the instrument's spectral transfer function. If the vertical distributions of temperature and constituent mixing ratios are suitably uniform and well known the ratio of radiances at the same wavenumber and azimuth angle but differing zenith angles could be a useful quantity.

The work presented here demonstrates the possibility of radiometric determination of temperature gradient magnitudes. Though not exact, the recovery scheme is based on well understood radiometric principles and is relatively simple to implement with proper equipment. While demonstrated here for a restricted range of wavenumbers the scheme shuold be readily extendable to other portions of the electromagnetic spectrum as different needs arise and as suitable hardware evolves.

REFERENCES

Arams, F. R., 1973: *Infrared to Millimeter Wavelength Detectors*. Dedham, Artech House.

Bignell, K., W. J. Burroughs, R. G. Jones, and H. A. Gebbie, 1969: A study of submillimeter atmospheric absorption using the HCN maser. *J. Quant. Spec and Rad. Trans.*, **9**, 809–824.

Burch, D. E., D. A. Gryvnak and R. R.Patty, 1966: Absorption of infared radiation by CO_2 and H_2O. Experimental techniques. *J. Opt. Soc.*, **57**, 885–896.

Cox, S. K., 1969: Observational evidence of anomolous cooling. *J. Atmos. Sci.*, **26**, 1347–1349.

Cox, S. K., 1973: Infrared heating calculations with an H_2O vapor pressure broadened continuum. *Quart. J. R. Met. Soc.*, **99**, 669–979.

Fleming, H. E. and D. S. Crosby,1978: New treatment of the boundary term in the inversion of the radiative transfer equation. In: Fymat, a. l. and V. Y. Zuyev (eds.), *Remote Sensing of the Atmosphere: Inversion Methods and Applications*. Amsterdam, Elsevier Scientific.

Goody, R. M., 1964: *Atmospheric Radiation, I: Theoretical Basis*. London, Oxford University Press.

Gradshteyn, I. S. and I. M. Ryzhik, 1980: *Table of Integrals, Products, and Series*. New York: Academic Press.

Herzberg, G. 1943: *Infrared and Raman Spectra*. Princeton, Van Nostrand.

Idso, S. B., 1980: On the systematic nature of diurnal patterns of differences between calculations and measurements of clear sky atmospheric thermal radiances. *Quart J. R. Met. Soc.*, **107**, 737–741.

Kondrat'ev, K. Y., 1973: *Radiation characteristics of the atmosphere and earth's surface* New Delhi, Amerind.

Kondrat'ev, K. Y., and Y. M. Timofeev, 1967: The applicability of approximation method for introducing atmospheric inhomogeneities into calculations of the transmissio functions of the rotational band of water vapor. *Izv., Atmos. and Ocean. Phys.*, **3** 226–244.

Kuhn, P., F. Caracena, and C. M. Gillespie, Jr., 1977: Clear air turbulence: detection b infrared observations of water vapor. *Science*, **196**, 1099–1100.

Kuhn, Nolt and Stearns, 1978: *Infrared passbands for clear-air-turbulence detection.* Optics Letters, **3**, 130–132.

Kuhn, P. M. and R. L. Kurkowski, 1984: Airborne infrared low-altitude wind shear detection test. *J. Aircraft*, **21** 792–796.

Liou, K. N., 1980: *An Introduction to Atmospheric Radiation.* New York, Academic Press.

Madden, R. P., 1961: A high-resolution study of CO_2 Absorption Spectra betheen 15 and 18 microns. *J. Chem. Phys.*, **33**, 2083–2097.

Stull, J. W., V. R. Wyatt and G. N. Plass, 1964: The infared transmittance of carbon dioxide. *Appl. Opt.*, **3**, 243–264.

Stull, J. W., V. R. Wyatt, and G. N. Plass, 1963: The infared absorption of carbon dioxide, infrared transmission studies. Vol. III, Rept. SSD-TDR-62-127, Space Systems Division, Air Force Systems Command, Los Angeles, CA.

Smith, W. L., 1969: A polynomial representation of carbon dioxide and water vapor transmission. ESSA Technical Report, NESC 47, Environmental Science Services Center, National Environmental Satellite Center.

Smith, W. L., 1970: Iterative solution of the radiative transfer equation for the temperature and absorbing gas profile of an atmosphere. *Appl. Opt.*, **9**, 1993–1999

Swihart, T. L., 1968: *Astrophysics and Stellar Astronomy.* New York: Wiley.

Ulaby, F. T., R. K. Moore and A. K. Fung, 1981: *Microwave Remote Sensing, Active and Passive., Vol. 1* Reading, Addison-Wesley.

Wang, W. and P. B. Ryan, 1983: Overlapping effect of atmospheric H_2O, CO_2 and O_3 on the CO_2 radiative effect. *Tellus*, **35B**, 81–91.

Wark, D. Q., 1961: On indirect temperature soundings of the stratosphere by satellites. *J. Geophys. Res.*, **66**, 77-82.

Appendix A

A POLYNOMIAL APPROXIMATION TO THE RADIATIVE TRANSFER EQUATION

Consider the radiative transfer equation in the form:

$$N(\phi) = A_1 \int_o^\infty dx \, \underbrace{B(\nu, T)}_{a} \, \underbrace{exp(\mathcal{T}(x))}_{b} \, \underbrace{\frac{d\mathcal{T}}{dx}}_{c} \tag{A.1}$$

Term a is the Planck function, b is the spectral transmissivity and term c is the effective weighting function. In the following discussion ∇T will be assumed to be the effective temperature gradient ∇T_{eff} as given by (6.1).

Define the reduced temperature gradient $\Phi = \frac{\nabla T}{T_o}$ where T_o is the temperature at the point of observation. With this, T(x) is given by

$$T(x) = T_o + x\nabla T = T_o(1 + \Phi x) \tag{A.2}$$

The Planck function can be approximated as:

$$B(\nu, T) = \beta_o + \beta_1 \Phi x \tag{A.3}$$

where $\beta_o = B(\nu, T_o)$ and $\beta_1 = T_o \frac{\partial B}{\partial T} \mid_{\nu, T_o}$

The optical thickness can be represented by

$$\mathcal{T}(x) = \int_o^x dx' \; q\rho(x')k(x') \tag{A.4}$$

with ρ the atmospheric density, q the mixing ratio of the emitting gas (assumed constant) and k the mass absorption coeffecient. Since density is a function of temperature only on a constant pressure surface,

$$\rho(x) = \frac{P}{RT_o(1+\Phi x)} \simeq \rho o(1-\Phi x)\ . \tag{A.5}$$

Assuming a Lorentzian line shape for the mass absorption coeffecient and using the approximation exploited by Smith (1968) and Kondrat'ev and Timofeev (1967), k(x) can be written as

$$k(x) = k(1 + (m+n)\Phi x) \tag{A.6}$$

where n = -1/2 is the pressure broadening factor and m is the result of the dependence of line intensity on temperature. Liou (1980) gives values of m = - 1 for CO_2 and m = -3/2 for water vapor. Combining the above expressions gives the approximate optical thickness:

$$\mathcal{T}(x) = \mathcal{M}\int_o^x dx' \; (1-\eta\Phi x') = \mathcal{M}(x - \frac{\eta}{2}\Phi x^2) \tag{A.7}$$

where

$$\eta = -(m+n-1) \quad \text{and} \quad \mathcal{M} = \mathrm{q}\rho_o\mathrm{k}_o$$

Also

$$\frac{d\mathcal{T}}{dx} = \mathcal{M}(1 - \eta\Phi x) \ . \tag{A.8}$$

In (A.7) and (A.8) terms involving nonlinear terms in Φ have been dropped.

Next consider the term:

$$exp\left(-\mathcal{M}(x - \frac{\eta}{2}\Phi x^2)\right) = exp(-\mathcal{M}x)exp(\mathcal{M}\frac{\eta}{2}\Phi x^2) \ . \tag{A.9}$$

The integral (A.1) will not converge with this exponential expression. Equation (A.9) is physically unrealistic however since it suggests a temperature gradient of infinite extent. More realistically the decaying exponential drives the integrand to very small values before the quadratic exponential term becomes large. Hence the quadratic term can be approximated as:

$$exp(\mathcal{M}\frac{\eta}{2}\Phi x^2) \simeq (1 + \mathcal{M}\frac{\eta}{2}\Phi x^2) \ . \tag{A.10}$$

Combining the results into (A.1) and again dropping all terms super-linear in Φ gives:

$$N(\phi) = A_1\mathcal{M}\int_o^\infty dx\ e^{-\mathcal{M}x}(\beta_o + (\beta_1 - \eta\beta_o)\Phi x + \beta_o\mathcal{M}\frac{\eta}{2}\Phi x^2) \ . \tag{A.11}$$

With the help of:

$$\int_o^\infty dx\ x^{\nu-1}\ e^{-\mu x}\ = \frac{1}{\mu^\nu}\Gamma(\nu)$$

(Gradshteyn and Ryzhik, 1980) the integral can be done. The result is:

$$N(\phi) = A_1\left(\beta_o + \frac{(\beta_1 - \eta\beta_o)\Phi}{\mathcal{M}} + \frac{\beta_o\mathcal{M}\frac{\eta}{2}\Phi}{\mathcal{M}^2}2\right) = A_1\left(\beta_o + \frac{\beta_1}{\mathcal{M}}\Phi\right) \ . \tag{A.12}$$

The correct value for the normalization constant A, in this simple constant pressure surface case is simply β_o^{-1}, the inverse of R(90°) and so (A.12) becomes:

$$N(\phi) = 1 + \frac{C_2 \nu \chi}{T_o^2} \frac{|\nabla T|}{2} cos\phi \, . \qquad (A.13)$$

Here the approximation has been made that $\frac{To \frac{\partial B}{\partial T}|_{\nu,T}}{B(\nu,To)} \simeq \frac{C_2 \nu}{T_o^2}$ and $\mathcal{M}\chi \equiv 2$ has also been used.